HfO_2-based ferroelectrics applications in nanoelectronics

Mircea Dragoman[1*], *Martino Aldrigo*[1], *Daniela Dragoman*[2,3], *Sergiu Iordanescu*[1], *Adrian Dinescu*[1], *Mircea Modreanu*[4]

[1]National Institute for Research and Development in Microtechnologies (IMT Bucharest), Erou Iancu Nicolae Street 126A, 077190 Voluntari (Ilfov), Romania

[2]Univ. of Bucharest, Physics Faculty, P.O. Box MG-11, 077125 Bucharest, Romania

[3]Academy of Romanian Scientists, Ilfov 3, 050044 Bucharest, Romania

[4]Tyndall National Institute-University College Cork, Lee Maltings, Dyke Parade, Cork, Ireland

Keywords: ferroelectrics, microwaves, 2D materials, 2D/ferroelectrics heterostructures, energy harvesting

This paper is dedicated to HfO_2-based ferroelectrics applications in nanoelectronics, especially to topics not well developed up to now, such as microwaves, energy harvesting, and neuromorphic devices working as artificial neurons and synapses. Other well-covered topics in literature, such as memories or negative capacitance ferroelectric field-effect transistors, will be only briefly mentioned. The main impact of HfO_2-based ferroelectrics is the possibility to use them for fabricating at the wafer level CMOS compatible high-frequency devices, such as phase-shifters, antenna arrays or filters with a high degree of tunability and miniaturization, as well as energy harvesting devices and neuromorphic key components. In addition, the recent transfer of two-dimensional materials on HfO_2 ferroelectrics has demonstrated new physical effects, such as opening a 0.2 eV bandgap in graphene monolayers, and allowed the manufacture of very high-mobility FETs based on graphene/HfZrO.

This article has been accepted for publication and undergone full peer review but has not been through the copyediting, typesetting, pagination and proofreading process, which may lead to differences between this version and the Version of Record. Please cite this article as doi: 10.1002/pssr.202000521.

1. Introduction

Hafnium oxide (HfO_2) is the dielectric commonly used in field effect transistors (FETs) fabricated in CMOS technologies and, as such, retrieved in any very large-scale integrated (VLSI) circuits. Examples of such circuits include microprocessors or complex analog integrated circuits found in daily applications, for instance in computers, smartphones, laptops, or incorporated in cars, airplanes or medical equipments. Since the discovery of HfO_2 as a dielectric for modern integrated circuits, increasing its permittivity was a leading research issue in itself because higher permittivity values allow decreasing the effective oxide thickness (EOT), and so the leakage current; this is especially important when billions of Si FETs are integrated on a single chip. The solution found to boost the permittivity of HfO_2 is represented by structural phase transformations [1]. HfO_2 has its lowest electrical permittivity ($\varepsilon_r \approx 18$) in its stable phase, which is the monoclinic phase. Higher permittivity values, of $\varepsilon_r \approx 27$ in the cubic phase and $\varepsilon_r \approx 70$ in the tetragonal phase, are achieved, nonetheless, in phases that are stable only at very high temperatures, exceeding 1700 ^oC. The decrease of these temperatures is possible, however, by HfO_2 doping. Thus, the cubic and the tetragonal phases were first obtained at lower temperatures via Y doping [1] and, respectively, Si doping [2], while a stable HfO_2 tetragonal phase at nearly room temperature was observed by growing HfO_2 via atomic layer deposition (ALD) and doping it with ZrO_2 [3], [4]. As described in the recent review [5], the stabilization of these phases is determined by the concentration of dopants, the annealing temperature, and the growing methods.

These initial investigations focused on increasing the permittivity of HfO_2 lead eventually to the discovery of the orthorhombic phase of HfO_2, which was associated with HfO_2 ferroelectricity [6], [7]. This phase is obtained under different growth conditions in the presence of dopants, including those mentioned above, and requires strict control of dopant concentration, temperature, and mechanical strain. The most used orthorhombic HfO_2-based ferroelectric, named further as HfZrO, is doped with Zr and is usually grown at the wafer level, up to 300 mm, using ALD. It thus

benefits from the state-of-the-art CMOS technology. More recently, using Zr doping and pulsed laser deposition (PLD) another, rhombohedral phase of HfO_2 was discovered to be also ferroelectric [7]. The rhombohedral or orthorhombic HfZrO are ferroelectrics with similar electric performances, the origin of stable ferroelectricity in both cases being due to the induced strain between the top and/or down substrates sandwiching HfZrO [8].

Doping or strain application modifies the atomic structure of a material and can induce a phase transition, in particular can induce ferroelectricity in HfO_2. Similarly, HfO_2 can transform into a weak magnetic material [9], [10] due to high oxygen deficiencies or other dopants, whereas an atomically thin semiconductor, MoS_2, can becoming ferroelectric by applying mechanical strain with the help of an atomic force microscope (AFM) tip. This last situation will be detailed in the next chapter.

The bottom and top electrodes encapsulating HfZrO play a crucial role in maintaining the stability of ferroelectricity in this material. A common configuration is Si/TiN/HfZrO/TiN, in which ferroelectricity is preserved by the tensile strain and thermal expansion mismatch (see [11] for details). HfZrO is ferroelectric when its thickness is, typically, 4-6 nm, its ferroelectricity being generally lost for thicknesses larger than 10 nm. However, it was demonstrated that very thick HfO_2, reaching 1 μm, doped with 7% Y is still ferroelectric when grown by PLD on a (111) $Pt/TiO_x/SiO_2/(001)Si$ substrate [12]. On the contrary, it was very recently shown that HfZrO with a thickness of only 1 nm is ferroelectric when grown by ALD directly on Si/SiO_2, without the wake-up effects encountered in the Si/TiN/HfZrO/TiN structures [13]. We have also adopted the growth of HfZrO directly on Si starting from 2017 [14].

A possible explanation of ferroelectricity in HfZrO grown directly on Si or Si/SiO_2 is the occurrence of a novel ferroelectric paracrystalline phase due to oxygen vacancies engineering during the ALD growth directly on Si. This particular paracrystalline phase is defined as having short- and medium-range lattice ordering, but lacking crystal-like long-range ordering, and is assumed to form by the interplay of a new rhombohedral polar R3m ferroelectric phase [8]

(evidenced typically at 30.5° in GIXRD measurements) with a minority orthorhombic $Pca2_1$ phase. In Fig. 1 we have represented the GIXRD pattern of the HfZrO thin film on Si(100), indicating the rhombohedral phase. Of course, more structural characterizations are necessary to validate this explanation.

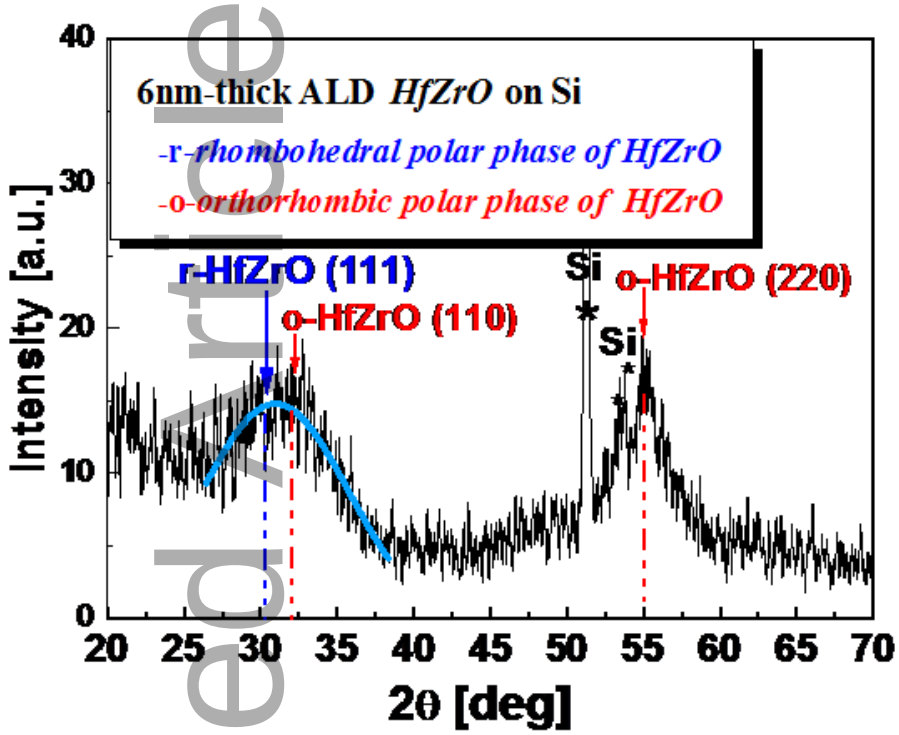

Fig. 1 GIXRD pattern of the HfZrO thin film on Si(100) indicating the rhombohedral phase (adapted from [14], Fig. 1(b)).

There are intensive researches regarding HfO_2-based ferroelectrics, such as those previously reported in the recent reviews [15],[16],[17],[18],[19],[20] which address applications of HfO_2-based ferroelectric memories [17], or negative capacitance ferroelectric FETs [18],[19],[20]. Therefore, we will not focus further on these issues but will concentrate in this review on the applications of HfO_2-based ferroelectrics in nanoelectronics, especially in microwaves, energy harvesting, and computing. Each application will start by highlighting the relevant physical properties of HfO_2 in that particular case. Nonetheless, there are some basic physical properties and

related parameters of HfO_2-based ferroelectrics, such as HfZrO, which are important for many applications, such that we list them from the beginning, in Table I.

Table I Basic physical properties of HfZrO and the nanoelectronic areas where they are applied.

Name	Value and units	Applications in nanoelectronics
Remanent polarization, P_r	10-40 $\mu C/cm^2$ [3]	in all applications, especially memories
Coercive electric field, E_C	2-4 MV/cm [3]	in all applications, especially memories, ferroelectric transistors,
Relative electrical permittivity, ε_r	20-40 [5]	tunable with applied DC, microwave, and optical applications

2. Atomically-thin ferroelectrics

Atomically-thin or two-dimensional (2D) ferroelectrics are the ultimate ferroelectrics consisting of one or few monolayers. 2D materials commonly originate from van der Waals materials, which consist of billions of monolayers bound together by (out-of-plane) weak van der Waals forces, strong bonds being encountered between atoms in such a monolayer (in-plane). Therefore, individual monolayers could be detached easily with a scotch tape, for instance, notorious cases in this sense being graphene and 2D dichalcogenides, such as MoS_2 [21]. Some 2D ferroelectrics, examples of which are mentioned in Table II, are obtained in a similar way. The most studied 2D ferroelectric monolayer is the recently discovered α-In_2Se_3 [22].

Table II 2D ferroelectrics (for more details, see [23],[24] and the references therein)

2D ferroelectric	Thickness (nm)	E_C (kV/cm)
$CuInP_2S_6$	50 nm	60
α-In_2Se_3	2-10 nm	20
SnS	Few monolayers	10.7

Note that all these 2D ferroelectrics reported in [23] and [24] are not CMOS compatible and are not grown at the wafer-scale until now, their ferroelectricity being evidenced either in-plane or out-of-plane depending on the material. On the other hand, HfO_2-based ferroelectrics are not van der Walls materials but are, however, CMOS compatible atomically-thin ferroelectrics and can be grown at wafer scale. We have shown recently that the 2D semiconductor MoS_2 (see Fig. 2), grown at the wafer-scale and having a thickness of 4.6 nm (7 monolayers), is also ferroelectric due to the applied strain [25].

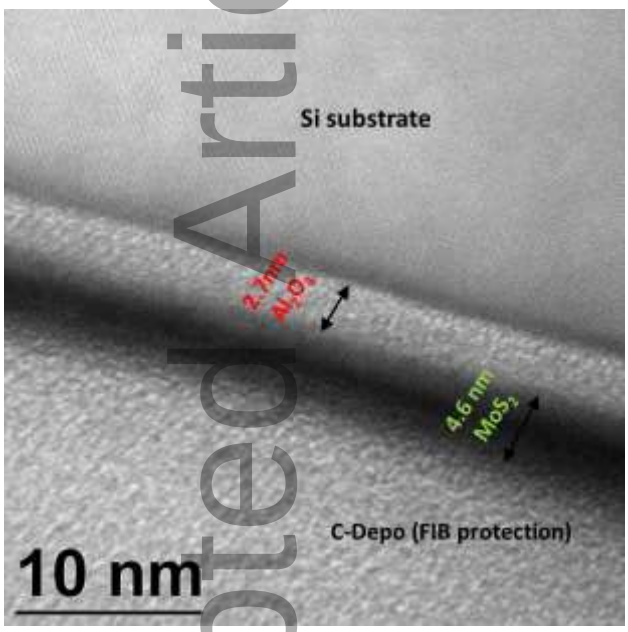

Fig. 2 HR TEM cross-section of the 4.6 nm-thick MoS_2 semiconductor ferroelectric [25].

To demonstrate the ferroelectricity of the ultrathin MoS_2, PFM spectroscopy curves were performed for various values of the AC voltage amplitude applied to the tip. Each plot of amplitude and phase was recorded by scanning the DC voltage between −10 V and + 10 V in both directions, at various points of the MoS_2 surface. Starting from an AC voltage amplitude of around 0.5 V (see Fig. 3), we observe that both amplitude and phase have a hysteretic behavior with a phase shift around 200 degrees, indicating the onset of ferroelectricity via strain. Beyond 0.8 V, the phase shift becomes 360 degrees and the ferroelectricity is lost.

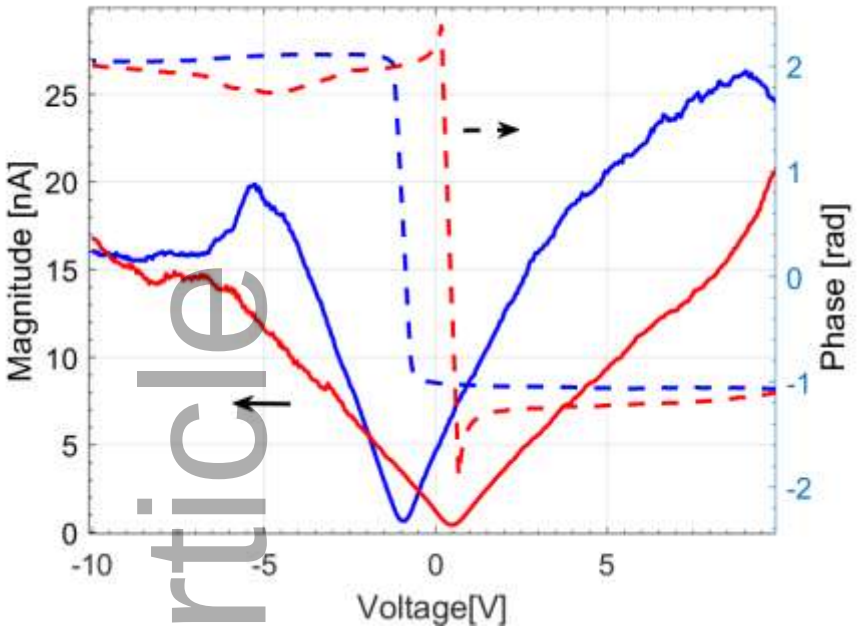

Fig. 3 Piezo-Force amplitude and phase curves obtained for 0.5 V AC voltage applied to the tip during PFM spectroscopy [25].

Future work is needed to investigate this material, especially regarding the suitable doping route of MoS_2 semiconductor and for identifying suitable capping layers in order for MoS_2 to become a stable ferroelectric with atomic thickness that can be grown at the wafer scale.

3. Microwave devices based on HfZrO

The tunability of devices and circuits at high frequencies is a prerequisite for further developments of radars and modern communications, such as 5G, internet, and Internet-of-Things (IoT), as well as for rapid changes in the environment properties or demands for various applications. The tunability is implemented at high frequencies using specific materials, in particular ferroelectrics [26]. However, in the case of the first ferroelectrics used in this frequency range, namely perovskite ferroelectrics, such as $Pb(Zr,Ti)O_3$ or PZT, the DC voltages necessary for tuning the frequency or the phase of microwave devices is very high, of tens and even hundreds of Volts. In addition, because perovskite ferroelectrics are not CMOS compatible and are difficult to grow at large wafer scales, the ferroelectric microwave devices were almost abandoned. Therefore, since HfZrO is

CMOS compatible and only a few Volts are necessary to tune a microwave device based on it, has a great potential for tunable microwave devices.

The most important property of any ferroelectric in microwave applications is the electrical permittivity dependence on the applied voltage at high frequencies. We have measured the effective permittivity and wave propagation constant of HfZrO in the frequency range 1-14 GHz using two coplanar lines (CPWs) with different lengths. We observed an increase of 27% of the effective permittivity when the applied voltage varies from 0 V to 5 V [27] and have also measured the attenuation constant, phase constant, and loss tangent of HfZrO up to 14 GHz. The fabrication of HfZrO CPWs implies the ALD growth of HfZrO with a thickness of 6 nm on a high-resistivity Si (HR Si) wafer with a thickness of 525 μm, followed by metal deposition of metallic CPWs using e-beam techniques. Various structural characterization techniques used to validate the ferroelectricity of HfZrO are presented in [27]. The CPW metallization consists of a 50 nm/500 nm thick Ti/Au layer, the width of both CPWs is W = 1 mm, whereas the lengths of the two CPWs are L_A = 6.671 mm and L_B = 2.393 mm. The CPW lines are depicted in Fig. 4.

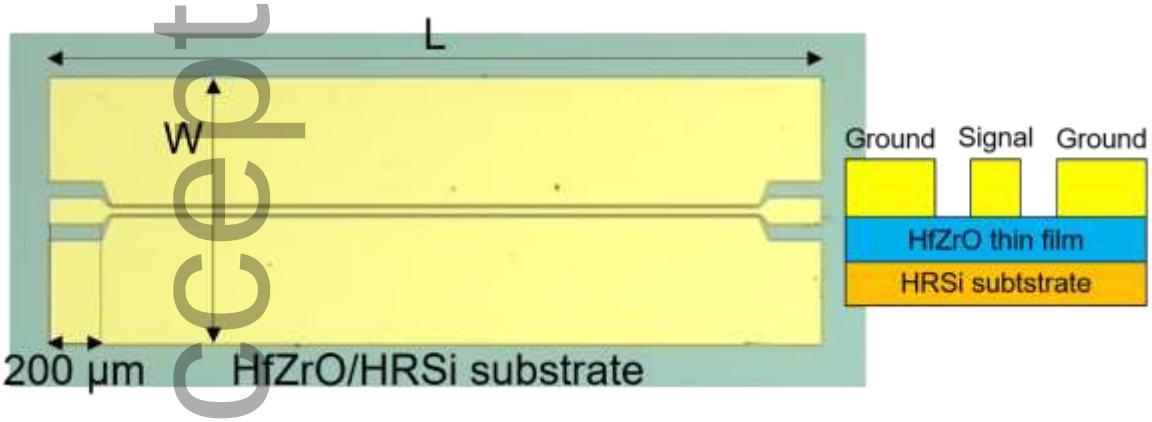

Fig. 4 The HfZrO/HRSi CPW top-view (optical image) and schematic cross-view section [27].

We have measured the S parameters of the CPWs, i.e., the return loss (S_{11} and S_{22}) and transmission (S_{21} and S_{12}), and we have extracted the effective permittivity using the Bianco-Parodi formula. The results are depicted in Fig. 5. The measurements are performed at room temperature

on-wafer using a vector network analyzer (VNA) Anritsu-37397D connected to a Karl-Suss PM5 probe station, while DC polarization is applied using the internal bias tees of the VNA.

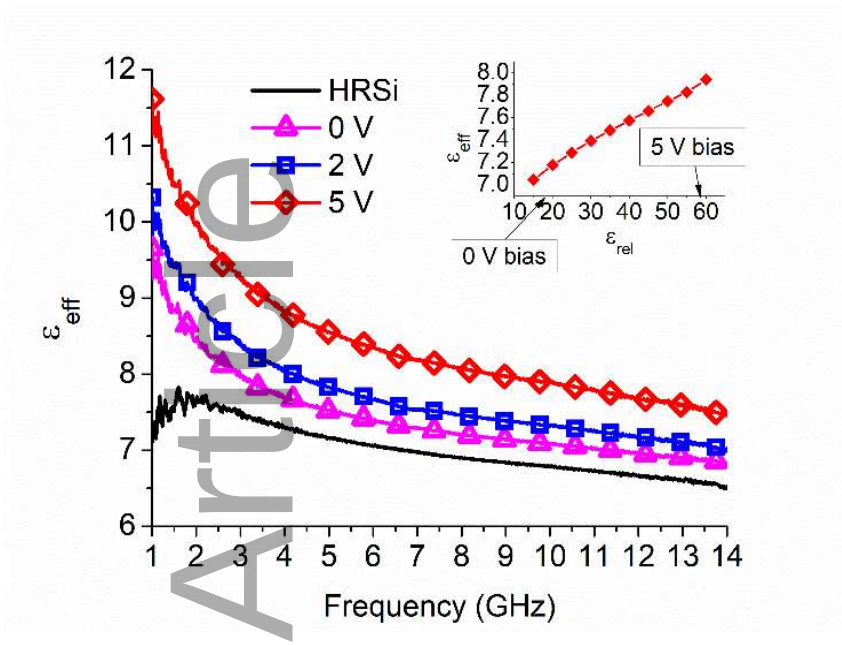

Fig. 5 The dependence of the effective permittivity of HfZrO CPW on frequency and that of effective permittivity versus relative permittivity obtained by a fitting procedure at 10 GHz [27].

From Fig. 5 it can be seen that at 2.45 GHz the relative effective permittivity is 7.61 at 0 V and 9.64 at 5 V, so the change in the DC voltage induces a change of 27% of the effective permittivity, while at 10 GHz the effective permittivity is of 6.79 at 0 V and 7.89 at 5 V, so that the increase of 27% of this parameter is almost constant within the range 2-10 GHz. The relative permittivity values reported in the literature were obtained using other methods [11]. We have found an empirical formula for the dependence of the relative permittivity of HfZrO in the microwave range depending on the microwave effective permittivity at 0 V, $\varepsilon_{eff}(0)$, and the substrate permittivity ε_S:

$$\varepsilon_r(E) = [\alpha(E - E_c)t + \varepsilon_{eff}(0)/(\varepsilon_S)^{1/2}]^2 + \varepsilon_{eff}(0) \quad (1)$$

where $\alpha \leq 1$ V^{-1}, E is the applied field, E_c is the coercive field, and t is the thickness of HfZrO.

We have then calculated the loss tangent tan δ at various frequencies and DC voltages using the microwave data. The results, illustrated in Fig. 6, show low values of tan δ and thus moderate losses of HfZrO in the microwave domain.

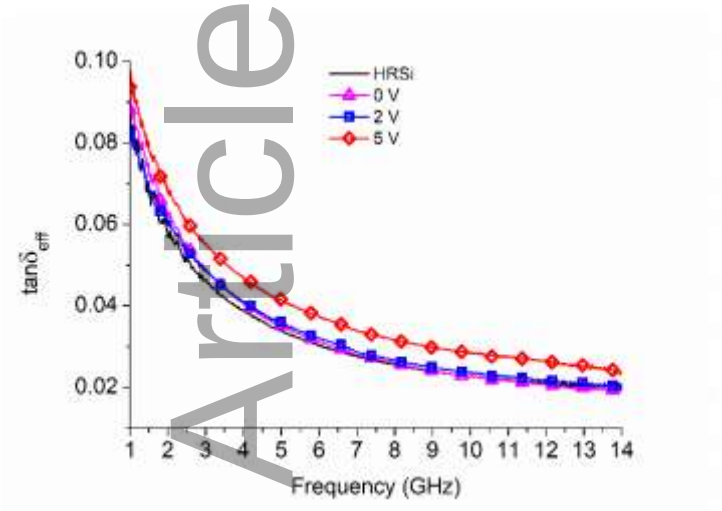

Fig. 6 The loss tangent tan δ of HfZrO in microwaves [27].

The phase shifter is a key device in phased antennas arrays. Ferroelectric phase shifters are tunable via applied DC voltages, with values of few V in the case of ultrathin HfZrO. We have shown that in a 1-mm-long gold CPW interdigitated structure deposited over 6 nm HfZrO grown by ALD directly on a high-resistivity Si substrate, the phase shift in microwaves is higher than 60^o at 1 GHz and of 13^o at 10 GHz at the maximum applied DC voltages, of ± 3 V [14] (see Fig. 7).

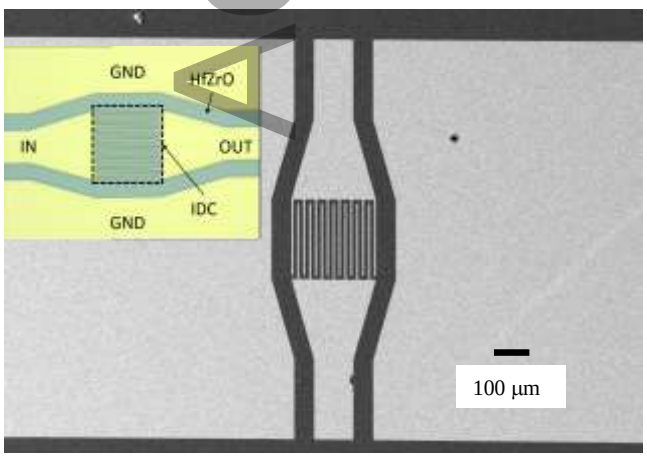

Fig. 7 The microwave HfZrO phase shifter [14].

Hundreds of phase shifters were fabricated on the same wafer, all showing similar characteristics. The bias is applied vertically on the CPW, such that HfZrO is polarized vertically. The phase shift of the microwave signal in the frequency domain 1-10 GHz is represented in Fig. 8 at various voltages, in the range ±3 V. We defined the phase shift as $\Delta\varphi = \varphi_{V_{DC}} - \varphi_{0V}$, i.e., as the difference between the phase at a certain DC voltage and that at 0 V for a given frequency value. Figure 8 shows that beyond ± 3 V the phase shift does no longer increase with the bias since the field becomes higher than the coercive electric field.

The capacitance of the phase shifter is defined as $C = -1/\omega\ \mathrm{Im}[\ Z_{in}(f, V_{DC})]$, with $Z_{in}(f, V_{DC})$ the input impedance. The capacitance decreases with frequency and increases with the applied voltage, increasing 4 times in the range 1-3 GHz. This behaviour explains the large phase shift, higher than 60^0/mm, obtained in this frequency range.

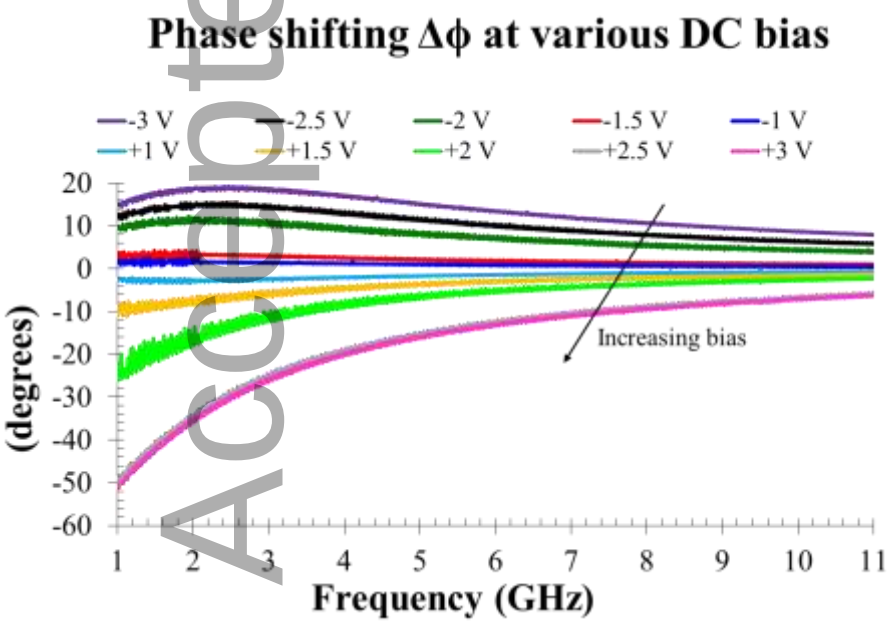

Fig. 8 The phase shift of HfZrO phase shifter [14].

The next step in extending the phase shifter application is to build an antenna array based on the above results. We have designed and fabricated at the wafer scale a phased array formed from

two gold antenna patches, phase shifters, and additional circuitry, all integrated on HfZrO/high-resistivity Si 4-inch wafer (see Fig. 9) [28]. We have observed that the radiation beam at 2.55 GHz is steered by 25º when HfZrO is biased with ±1 V, meaning that the phased antenna array can be biased with a simple battery. The phase shifters in Fig. 9 are the two interdigitated structures exciting the antennas.

On the same wafer with the antenna array, we have designed and fabricated another configuration including also coplanar lines and other phase shifters to verify separately the phase-shifting effect, i.e., to check if the microwave signal is shifted when a DC voltage is applied. Although the results are not different from those reported for the HfZrO phase shifter alone, a more careful design lead to a maximum phase shift of 53.74º at 2.55 GHz when sweeping the DC voltage between -1 V and + 1V.

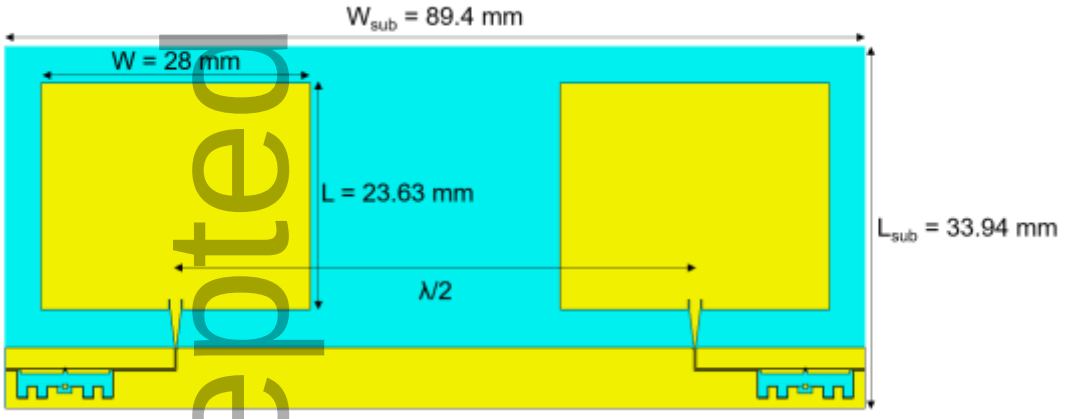

(a)

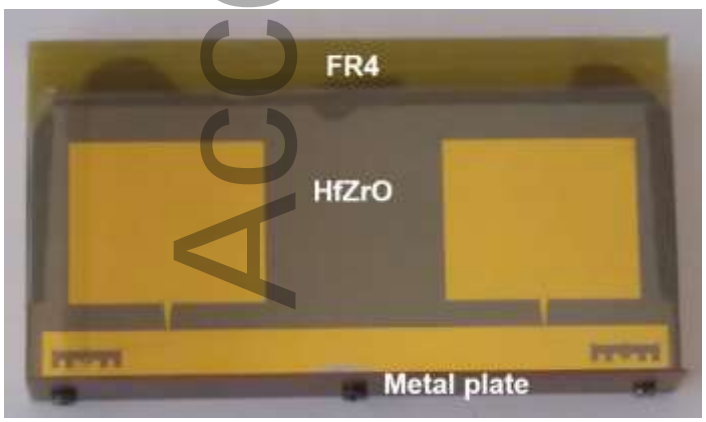

(b)

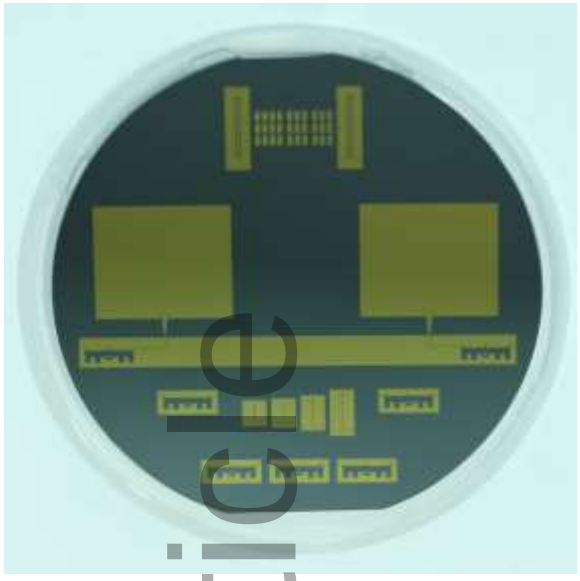

(c)

Fig. 9 The HfZrO antenna array: (a) design, (b) fabrication, (c) the HfZrO wafer [28].

We have measured the radiation pattern of the configuration in Fig. 9 in the range -30º and +30º, with steps of 5º, using as receiver a spectrum analyzer (Anritsu MS2668C 9 kHz-40 GHz) connected to a commercial 16 dBi gain reference antenna located on a rotating arm, while the HfZrO-based antenna array was placed at 1.2 m from the reference antenna (see Fig. 10).

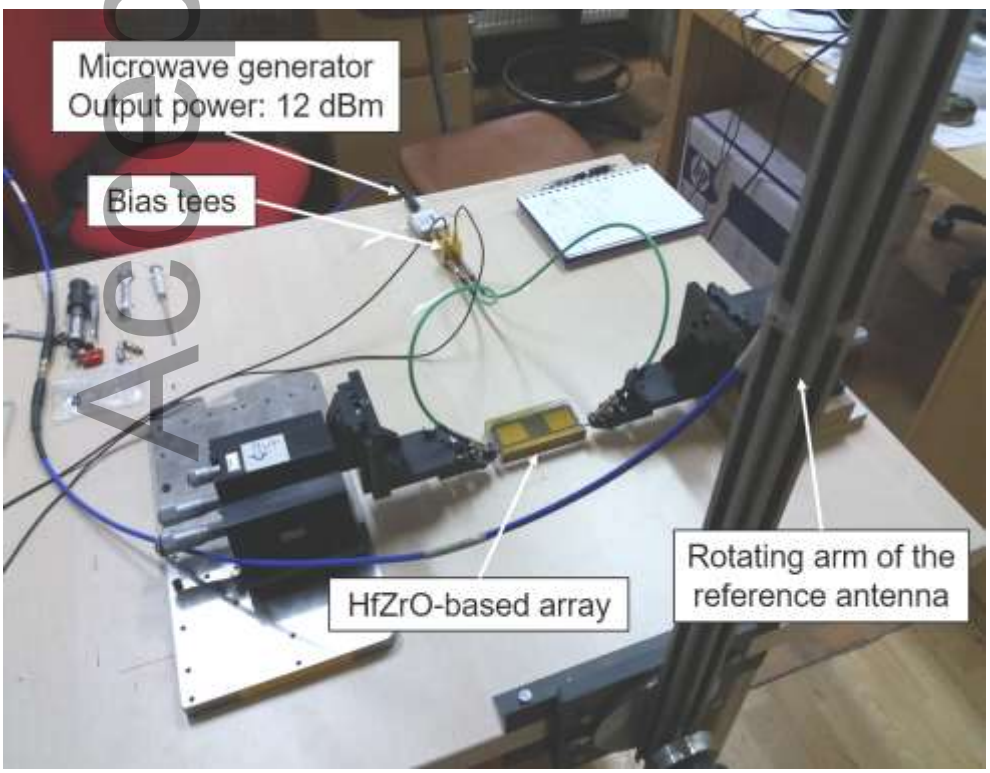

Fig. 10 The measurement set-up of the HfZrO antenna array [28].

We have found that the gain has a maximum value of 5.36 dBi. The steered radiated field is due to applying different DC biases on the two arms, which confer a maximum phase shift. In particular, after applying 0 V on both antennas, then -1 V to one patch and +1 V to the other one, we have observed that the radiation pattern is steered with 25^{o} at 2.55 GHz.

Very recently, we have shown that microwave filters based on a 6-nm-thick HfZrO layer are tunable in the range 0.1–16 GHz by varying the DC voltage in the range 0–4 V [29]. Three filter configurations: low-pass (LPF), high-pass (HPF), and band-pass (BPF) were designed, fabricated, and measured, showing a frequency shift of the minimum of the reflection coefficient between 90 MHz and 4.4 GHz, with a minimum insertion loss of about 6.9 dB in the high-pass configuration. The filters are illustrated in Fig. 11. All filters are made using inductors and interdigitated capacitors, which play the role of variable capacitors (varactors) due to the HfZrO ferroelectric layer underneath. The LPF and HPF have a T-network configuration: LPF is formed from two series inductances and a shunt varactor and HPF consists of two series varactors and a shunt inductor, while the BPF results from the connection of the LPF to the HPF. As a major result, the BPF has much lower dimensions (3.19 mm × 3.47 mm) than the working wavelength.

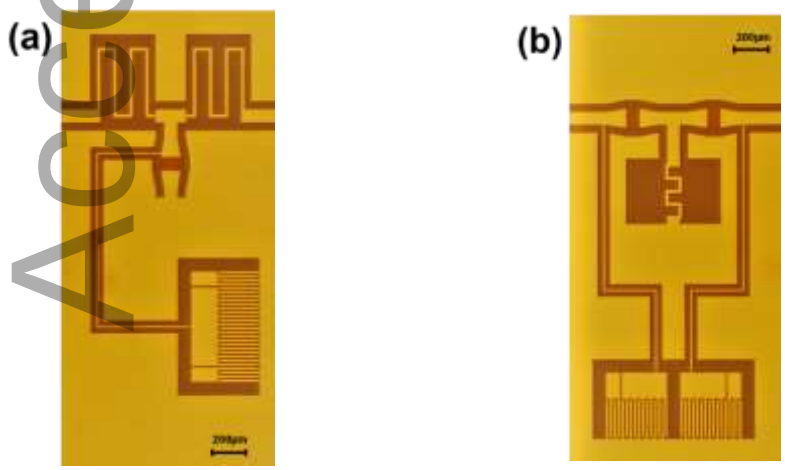

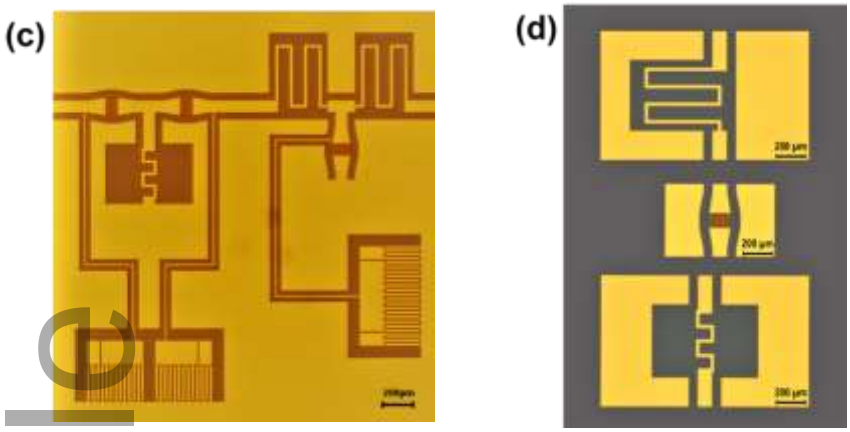

Fig. 11 The optical image of (a) LPF, (b) HPF, (c) BPF, and (d) test structures [29].

From the above figure it follows that all structures contains separate inductors and capacitors that must be tested before the measurement of the filters. The interdigitated capacitance, C_{IDC}, and phase, ϕ_{IDC}, in the CPW configuration versus the applied DC voltage for the frequencies of 2.5 GHz, 5.5 GHz, and 10 GHz are represented in Fig. 12. At 2.5 GHz, the capacitance increases from 0.38 pF to 0.58 pF as the DC voltage is swept from 0.5 V up to 4 V, whereas during the same DC voltage sweep the phase decreases from 48.7° to 34.7°, resulting thus a phase shift of 14°. By increasing the frequency to 10 GHz and by tuning the DC voltage in the same range, the capacitance increases from 0.28 pF to 0.33 pF, while the phase decreases from 11.76° to 5.86°, i.e., the obtained phase shift is now of about 6°. This microwave measurement demonstrates that HfZrO is acting as ferroelectric at very high frequencies, including the X band.

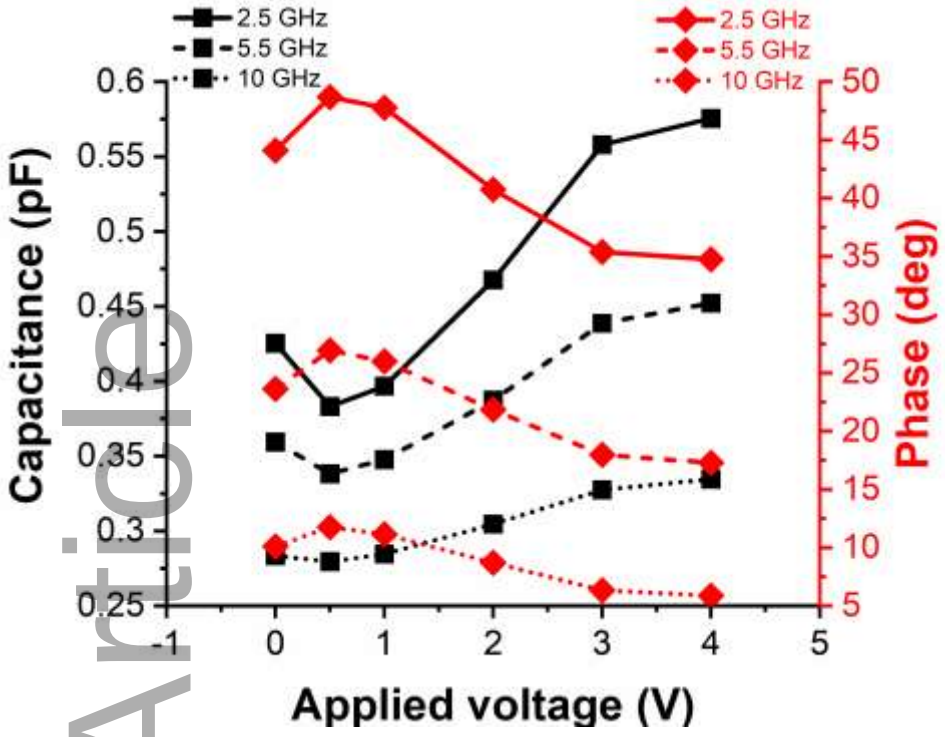

Fig. 12 The capacitance and phase of the CPW interdigitated capacitor acting as a varactor versus the applied DC field at various frequencies [29].

The frequency shifts (Δf) of the three types of HfZrO filters is shown in Fig. 13. In the case of LPF, the maximum Δf is 4.5 GHz, while this parameter is 1 GHz for HPF and 2.5 GHz for the BPF. The frequency shift is caused by the HfZrO ferroelectric thin film, since the change of maximum 8% of the effective permittivity, corresponding to 65% variation of the relative permittivity via formula (1) produces a phase shift of the microwave signal propagating through the filter, while the impedance is still matched to 50 Ω.

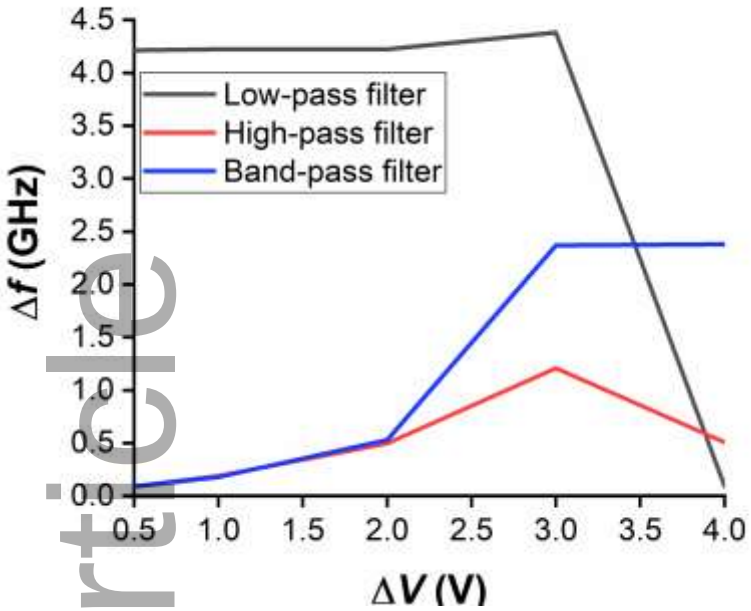

Fig. 13 The frequency shifts (Δ*f*) of the three filters versus applied DC voltage at 10 GHz [29].

The most significant results are obtained for the HPF. Figure 14 displays the frequency dependence of the transmission coefficient at 3 V, showing that the rejection with respect to the central frequency of 10 GHz, is about 8.7 dB at 6 GHz, 13.2 dB at 4 GHz, and 24 dB at 2 GHz. We note here that all the filters have much smaller dimensions than the wavelengths of working frequencies. For example, the BPF – the largest filter – has dimensions of 3.19 mm × 3.47 mm.

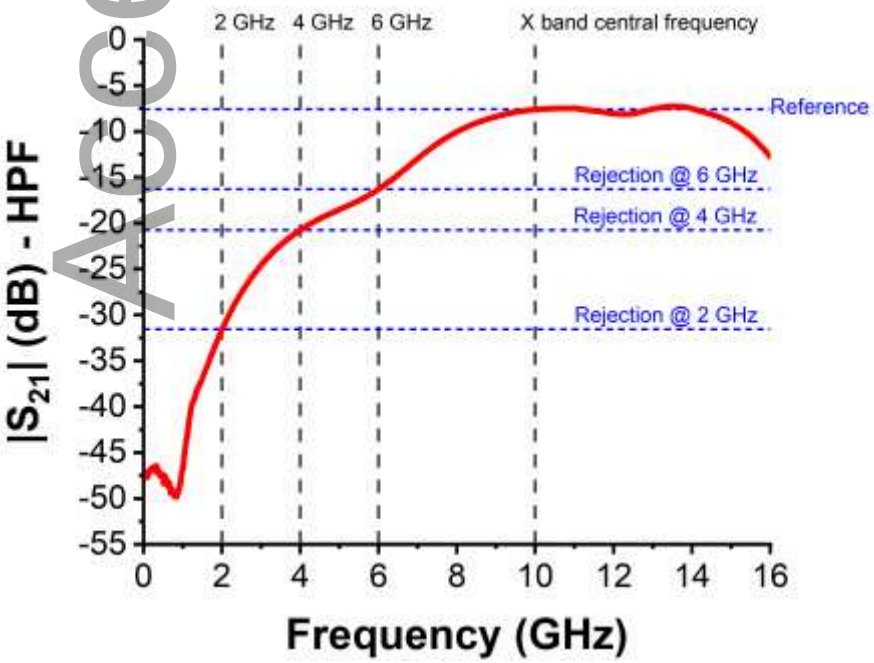

Fig. 14 Transmission coefficient $|S_{21}|$ for the HPF at 3 V [29].

4. 2D materials/ HfZrO heterostructures

All ferroelectrics, including HfO_2-based ferroelectrics grown via ALD, have a very small root-mean-square (RMS) surface roughness and are probably among the best substrates on which atomically thin materials can be transferred. In particular, HfZrO has a roughness of 0.2-0.3 nm [30], while this parameter is 0.4-0.6 nm in the case of hexagonal boron-nitride [31] and is bigger, around 1 nm, for SiO_2 [32]. Moreover, HfZrO is not only among the best substrates to transfer on graphene monolayers grown by CVD at the wafer scale, but, as we have shown very recently theoretically [33] and experimentally [34], HfZrO is opening a bandgap in graphene, conferring switching properties to FETs based on graphene monolayers. This implies that these FETs can be in well defined on and off states, paving the way for using graphene FETs in very fast logical circuits, since graphene on HfZrO has also a very large mobility, of 7900 cm^2/Vs at room temperature . The bandgap opening in graphene transferred on a HfZrO substrate, of around 0.2-0.4 eV, is due to orbital hybridization and local deformation of the graphene lattice. In all cases described below, the graphene monolayer is transferred by Graphenea on 4-inch wafers of $HfZrO/Al_2O_3/Si$ or $HfZrO/SiO_2/Si$, where HfZrO has a thickness of 6 nm. The fabrication of these structures implies several steps: (i) graphene channel patterning by e-beam lithography and reactive ion etching (RIE) (see Fig. 15(a)), (ii) source (S) and drain (D) patterning, metallization, and liftoff (see Fig. 15(b)); the channel length of the FET is 600 nm and has a width of 1 μm, (iii) gate (G) insulator deposition and patterning with 40-nm-thick HSQ (hydrogen silsesquioxane), as shown in Fig. 15(c), and (iv) metallic gate deposition (see Fig. 15(d)). More details about structural characterization and fabrication at the wafer level are found in [34]. The scanning electron microscopy (SEM) image of the graphene/$HfZrO/SiO_2/Si$ FET is displayed in Fig. 16.

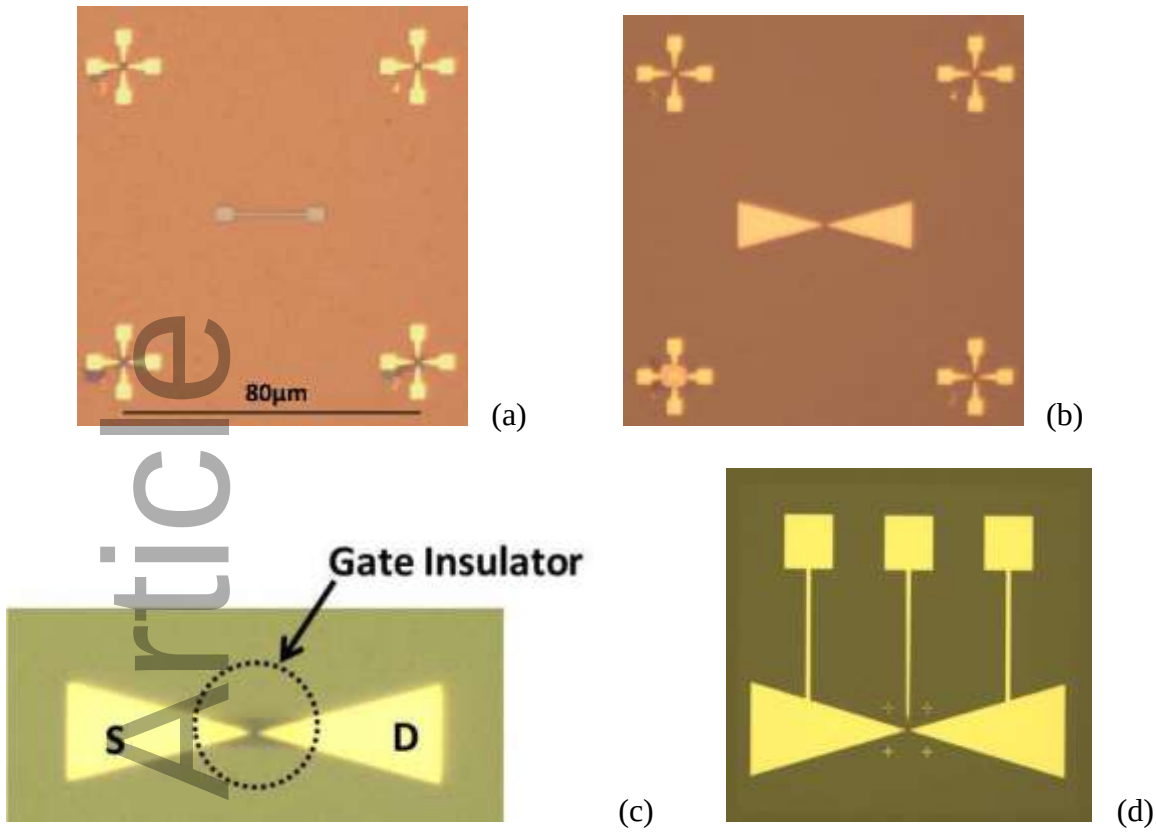

Fig. 15 Optical images of the graphene/HfZrO FET at various fabrication steps: (a) graphene channel patterning, (b) S and D fabrication, (c) gate dielectric deposition, and (d) FET electrodes deposition [34]

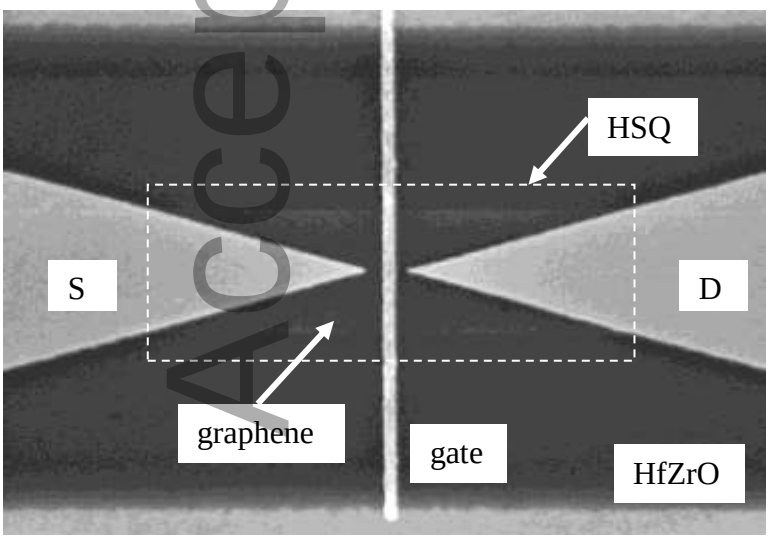

Fig. 16 The SEM image of graphene/HfZrO/SiO_2 /Si [34].

The drain current (I_D) versus drain voltage (V_D) at various gate voltages (V_G) for the structure in Fig. 16 is represented in Fig. 17 with corresponding error bars. When the gate voltage is increased beyond few volts, the drain current is decreasing until at V_G = 10 V the transistor reaches its off state; the leakage drain current is of 1 μA at a drain voltage of 3 V.

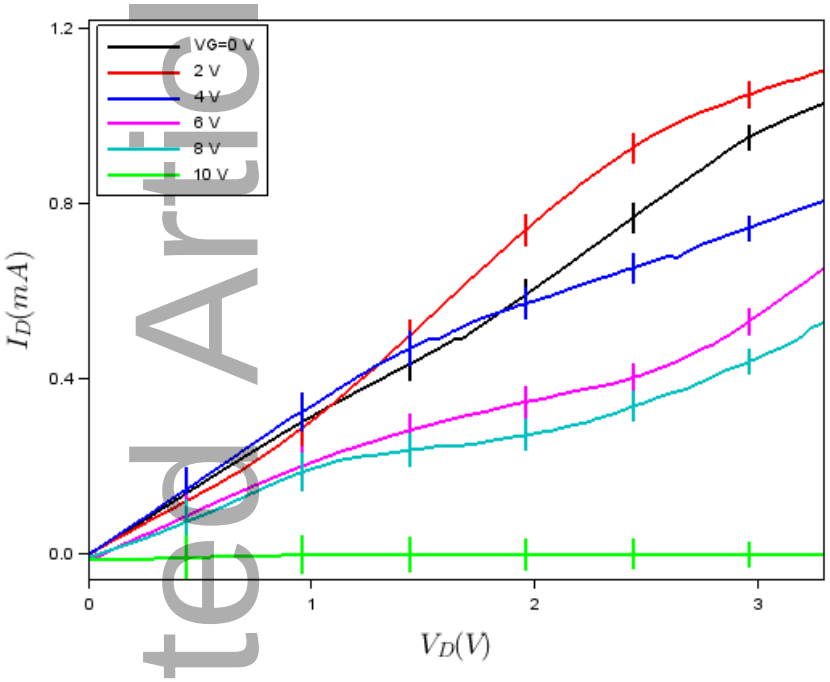

Fig. 17 Drain current versus drain voltage at various gate voltages [34].

The existence of a bandgap in the graphene/HfZrO/SiO_2/Si FET is demonstrated from the fact that the transistor is in an on state (for instance, at a gate voltage of 2 V) and in an off state, at a gate voltage of 10 V. We can determine the bandgap from the dependence of I_D versus drain gate voltages V_G at various drain voltages V_D, as displayed in Fig. 18 with corresponding error bars. The error bars in both Figs. 17 and 18 were considered from the measurements of 20 devices. From this figure it follows that there are three orders of magnitudes between the drain currents in the on and off states when the gate voltage is varied between -2 V and 2 V. For instance, at V_D = 0.5 V, $I_{D,on}$ is 0.24 mA at V_G = -2 V and $I_{D,off}$ = 0.22 μA at V_G = 1.5 V. Using the relation $I_{D,on} / I_{D,off} \propto \exp(E_g / k_B T)$ where k_B is the Boltzmann constant, we find that the bandgap E_g at

room temperature is about 0.18 eV. This bandgap value is comparable with that predicted by first-principle studies [33].

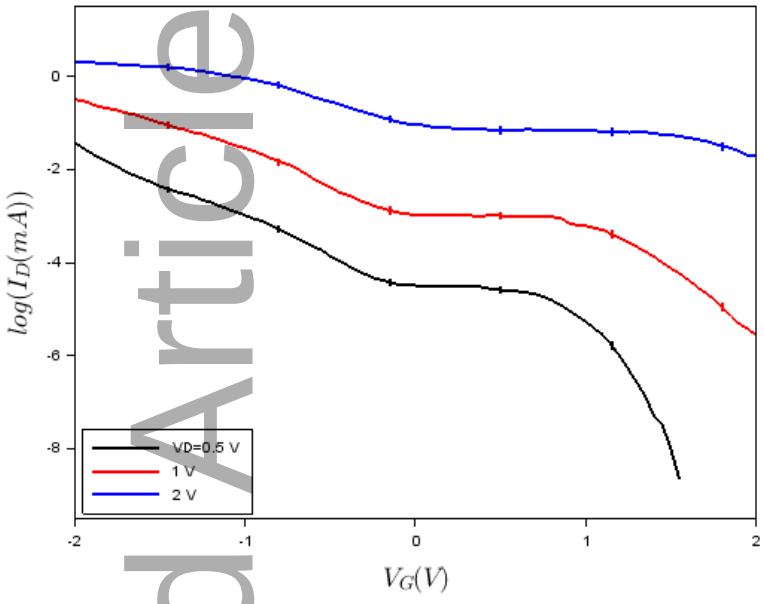

Fig. 18 Drain current versus gate voltage at various drain voltages [34].

Based on this research, we have shown that graphene/HfZrO FETs are memtransitors if the graphene channel is perforated with nanoholes having a diameter of 20 nm [35] or has as channel a graphene monolayer transferred on the 3-layers ferroelectric structure HfO_2/Ge-HfO_2/HfO_2 [36]. In principle, memristors are two-terminal devices, which are resistive non-volatile memories, having two distinct states, on and off, displaying different hysteresis loops of current-voltage dependence at repetitive sweeps of the voltage. Two-terminal memristors are represented mainly by valence change memristors (VCM) or filament memristors, which are metal-insulator-metal (MIM) structures, where the insulator is an oxide, such as TiO_x, HfO_x, or a 2D material [37],[38],[39]. Memtransistors, on the other hand, are active three-terminal devices based on FETs, having clear advantages over two-terminal memristors, such as: (i) no electroforming process for the wake-up,

(ii) tunable memory functions, (iii) high on-off ratios, and (iv) no sneak paths in crossbar arrays. Any memtransistor is an artificial synapse.

The first memtransistors, fabricated on flakes of MoS_2, worked initially at a drain voltage of 80 V [40], which was reduced progressively up to 12 V using different methods [41],[42], but remained still too high to be used in neuromorphic applications. In contrast, the ferroelectric memtransistors based on the HfO_2/Ge-HfO_2/HfO_2 3-layers-structure [36] are working at drain voltages in the range of -2 to +2 V and are fabricated at the wafer level. In Fig. 19 we present the cross-section of the HfO_2/Ge-HfO_2/HfO_2 FET memtransistor and in Fig. 20 the optical image of the HfO_2/Ge-HfO_2/HfO_2/Si chip.

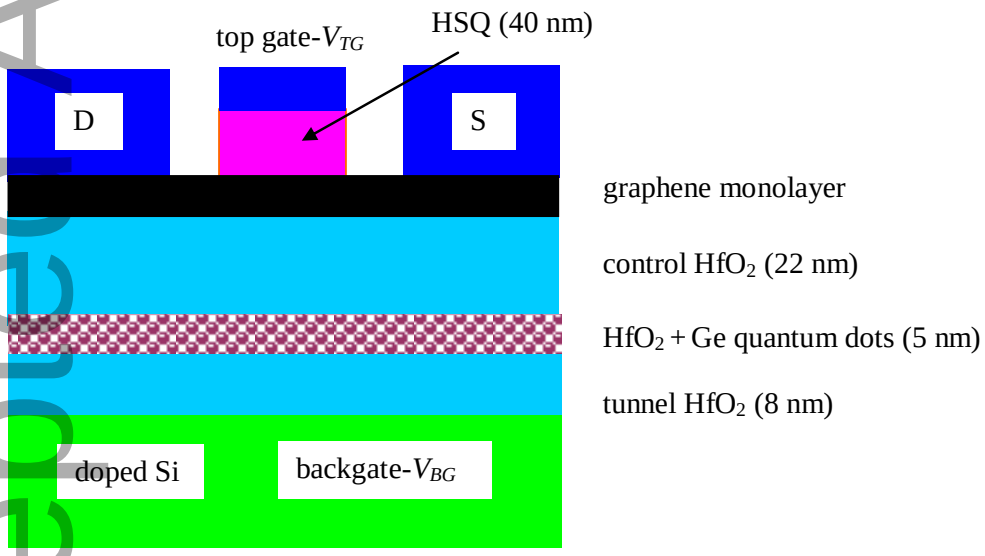

Fig. 19 The cross-section of the ferroelectric HfO_2/Ge-HfO_2/HfO_2 FET memtransistor [36].

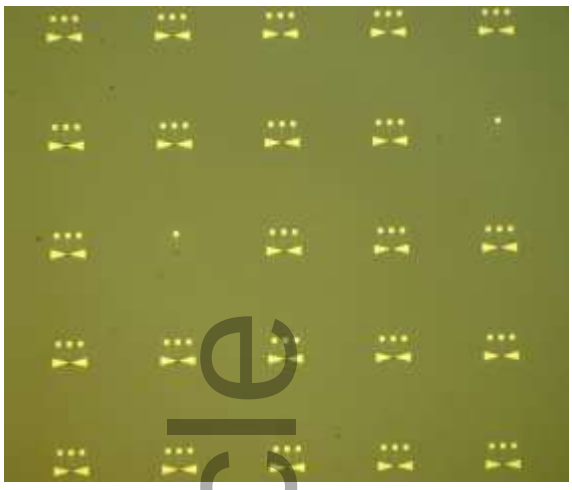

Fig. 20 The optical image of the ferroelectric HfO_2/Ge-HfO_2/HfO_2 FET memtransistors chip.

Any ferroelectric memtransistor has two main functions. First, it works like a three-terminal memristor when we consider the drain current versus drain voltage at various top-gate voltages (V_{TG}) and back-gate voltage (V_{BG}). In Fig. 21 we have represented, with corresponding error bars, I_D versus V_D at various top gate voltages when V_{BG} = 0. This figure illustrates the unique imprint of any memtransistor, namely a rotating hysteresis behavior at various gate voltages. The error bar is considered from the measurements of 7 devices.

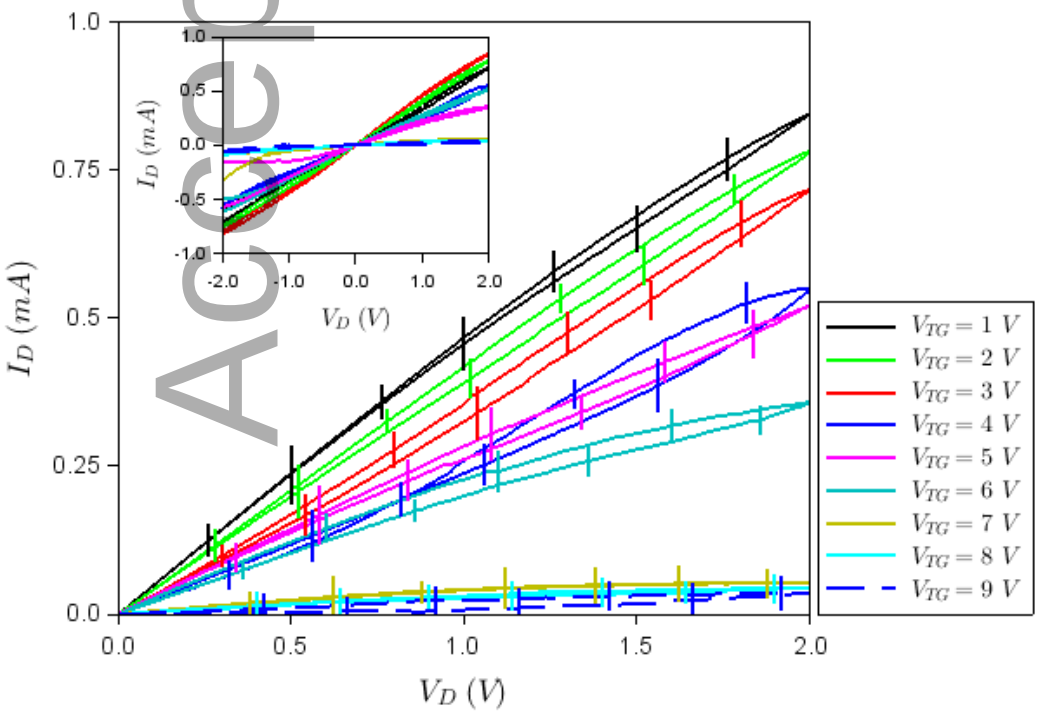

Fig. 21 I_D versus drain voltage (V_D) at various top-gate voltages (V_{TG}). Inset: the same dependence for both V_D polarizations [36].

Looking at the same I_D–V_D dependence in the logarithmic scale, we observe 12 orders of magnitudes difference between an off state (at V_{TG} = 9 V) and an on state (at V_{TG} = 1 V), so that the memtransistors can function as a logic element. It was shown recently that a transistor having an atomically thin material as a channel and both a top and a back gate can act as a logic device, whereas two FETs are needed in the case of Si technology to implement a single logic device. This simplification of the design of logic gates is possible since in the first case the carriers in the channel can be controlled independently by the two gates, which form in fact two surface channels [43]. The two inputs of the single device performing logic operations are in this situation the two gate voltages and the output is the drain current, which could be in a high or low state. In Fig. 22 we have displayed the dependence $I_D - V_{TG}$ for different back-gate voltages V_{BG}, for V_D = 1 V. All the dependencies show hysteretic behavior in the clockwise direction. Whether this figure shows that I_D is in a high or a low state depending on the back and top gate voltages, the building of a logic device based on these results is still under consideration at the present moment.

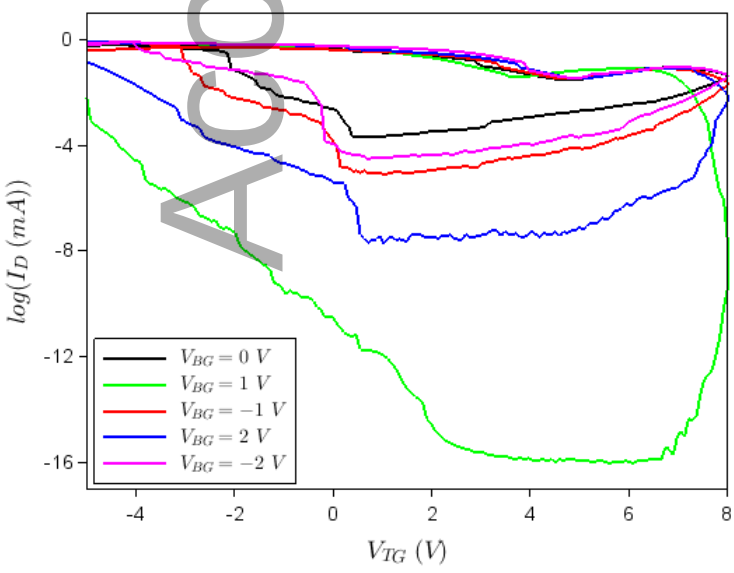

Fig. 22 $I_D - V_{TG}$ for different back-gate voltages V_{BG} on a semi-logarithmic scale [36].

5. Energy harvesting using HfO_2-based ferroelectrics

Energy harvesting is one of the areas of research that has been developed in the last years. It aims at collecting energy using various electronic devices for self-powering of sensors arrays and many tiny devices interconnected between them – the Internet-of-Things (IoT). Therefore, all types of ambient energies such as RF energy, heat, light, or mechanical vibrations are intended to be transformed and stored in electrical energy to power IoT [44].

Electromagnetic energy harvesting in microwaves and millimeter-waves domains is based on an antenna or an antenna array terminated with a diode having the role of rectifying the electromagnetic field at zero bias. The antennas integrated with a diode are referred to as rectennas. We will present in the following two types of rectennas. The first one is based on a MIM structure where the insulator is HfO_2 while the other is based on a ferroelectric HfZrO tunneling junction (FTJ). In the case of the harvesting based on rectification, the fact that HfO2 is ferroelectric or not is less important, the most important issue is a strong nonlinear current-voltage dependence which ensure a good yield for the microwave to DC conversion without any applied bias. Moreover, there are many reports indicating the undoped HfO2 is ferroelectric. Both structures are vertical and the rectification mechanism in both cases is the tunneling of carriers in HfO_2, with a thickness of 6 nm between top and bottom metallic electrodes. The first rectenna is based on the HfO_2 MIM diode and is represented in Fig. 23 [45]. We present integrated rectennas fabricated at the wafer level. The rectenna consists of a bow-tie antenna integrated with an Au/HfO_2/Pt MIM diode for electromagnetic harvesting in the 60 GHz bandwidth allocated to IoT. The top and bottom electrodes of the HfO_2 MIM diode form the bow-tie antenna arms. The area occupied by the bow-tie antenna is 20.25 mm^2 and its length is of 1.54 mm. The substrate is high-resistivity silicon (HR Si) having a thickness of 525 μm, over which a 300-nm-thick film of silicon dioxide (SiO_2) was deposited.

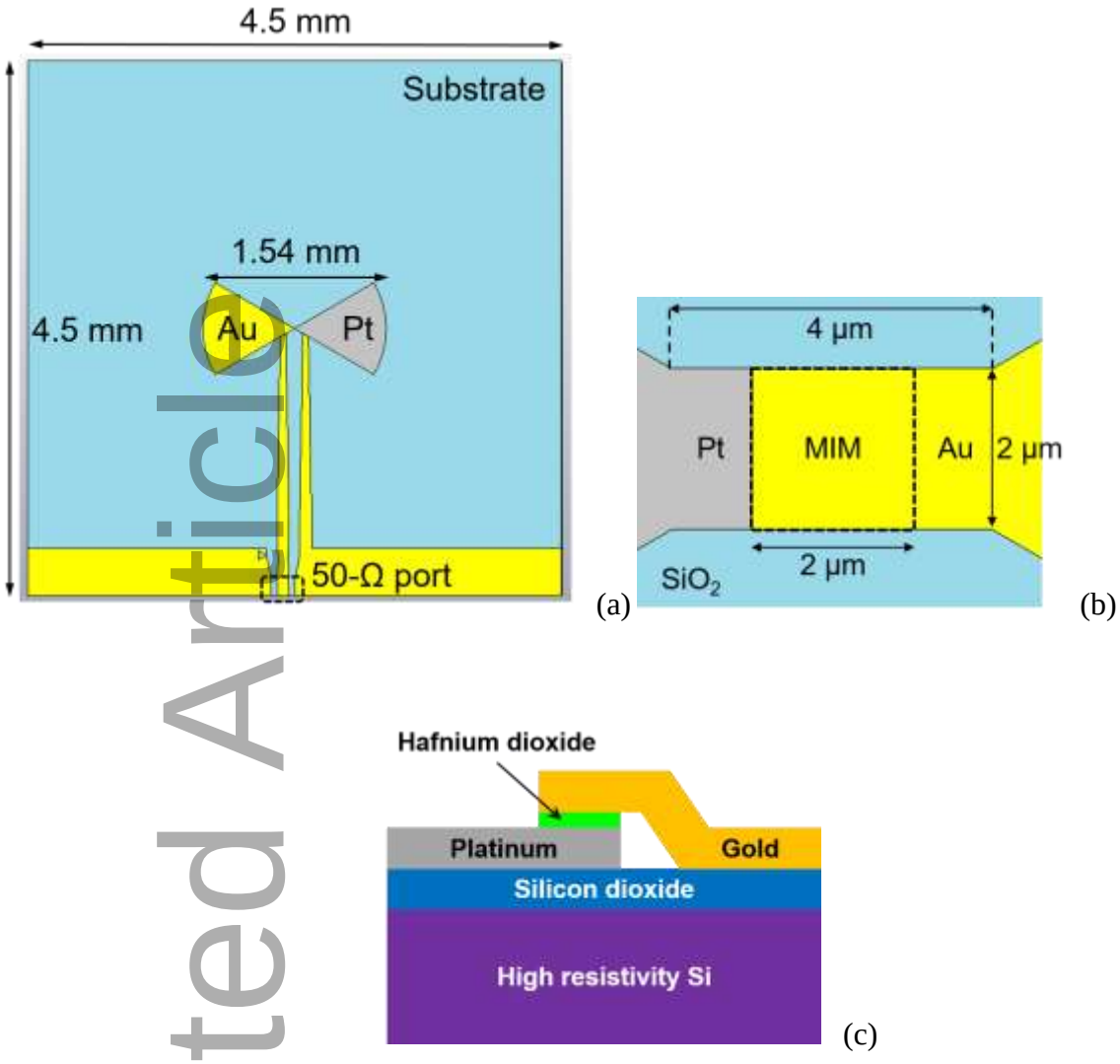

Fig. 23 The HfO_2 rectenna: (a) top-view of the bow-tie antenna and (b) MIM area; (c) cross-section of the MIM diode [45].

The rectenna output is fabricated in CPW technology for 50 Ω impedance matching. The fabrication process is explained in detail in [45]. In Fig. 24(a) we have represented the SEM image of the bow-tie antenna in the region of the MIM diode, while Fig. 24(b) illustrates the current-voltage dependence of this diode.

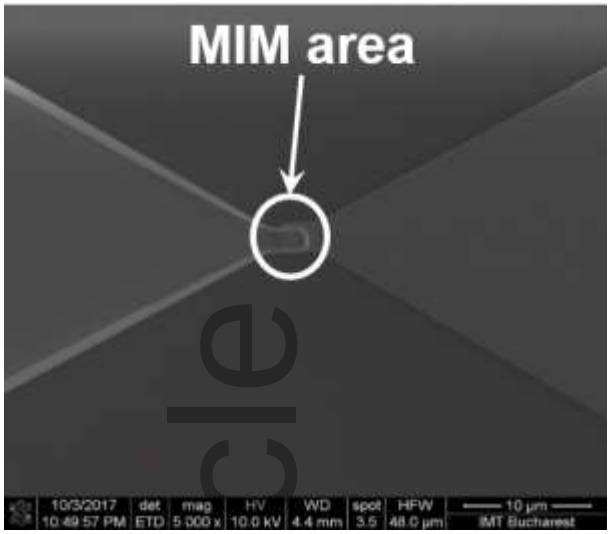

(a)

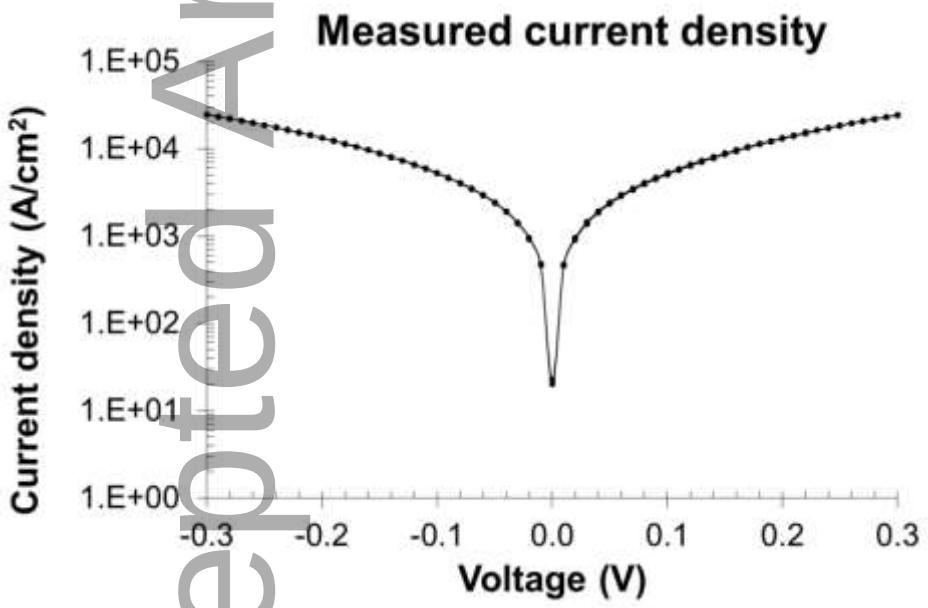

(b)

Fig. 24 (a) SEM image of the rectenna and (b) current density versus voltage of the MIM diode. [45]

Amplitude-modulated input signals having a continuous wave (CW) carrier at 61.6 GHz with 1 kHz rate are detected by this rectenna having no DC polarization (see Fig. 25). The harvested signal decreases in amplitude as the distance between the transmitter and the bow-tie is increased from 5 λ to 18 λ (see Fig. 25). We can thus harvest 250 µV at a distance of 5λ from the mm-wave transmitter, our wireless harvester having a responsivity of 5.4 V/W at an incident power of -20 dBm. Similarly, we have demonstrated that a metal-ferroelectric-semiconductor device coupled

to an antenna array can harvest electromagnetic energy at 26 GHz with a responsivity of 63 V/W and a NEP (noise equivalent power) of 4 nW/Hz$^{0.5}$, the harvested power being high enough to feed tiny things with a very low power consumption connected in an IoT network [46].

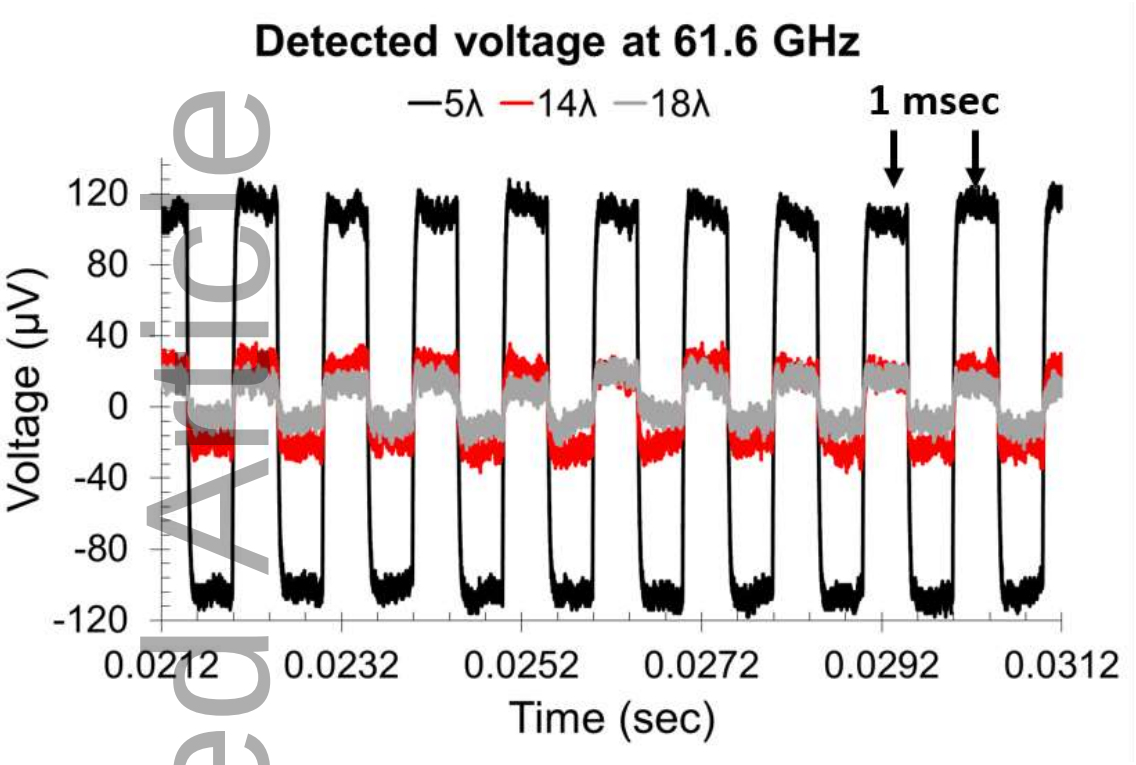

Fig. 25 The harvested signal from a 61.6 GHz wireless source which is AM modulated.[45]

The ferroelectric tunneling junction (FTJ) configuration is depicted in Fig. 26(a) and its current-voltage dependence in Fig. 26(b). The current-voltage (*I*–*V*) characteristic is obtained in the following way: before measurement, a poling signal – a ramp of +10 V – was applied, and then the *I*–*V* dependence was measured in the on state (black line). Subsequently, the polarity of the poling signal was reversed (-10 V), and after the poling signal was stopped the FTJ was measured in the off state (red line).

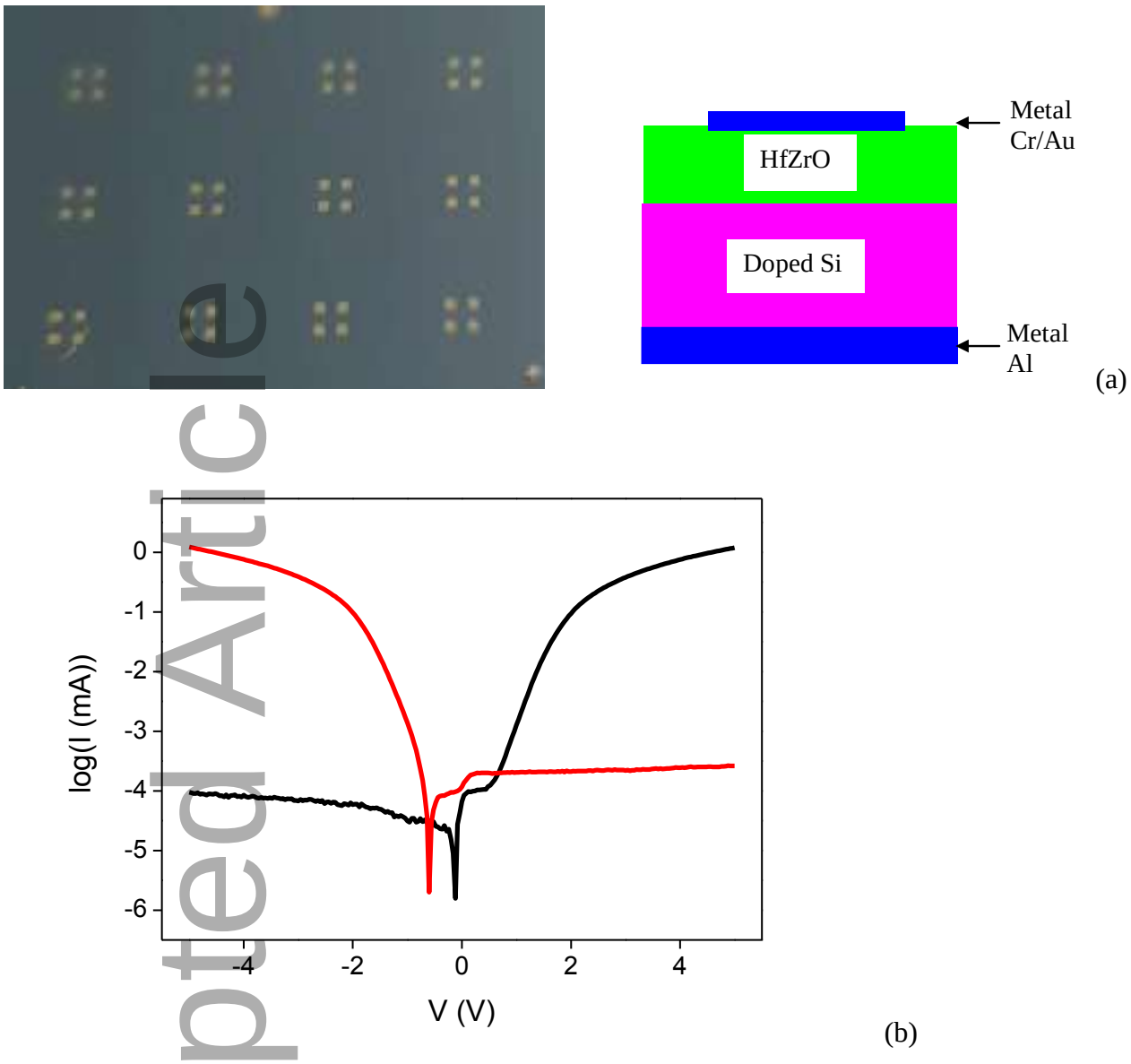

Fig. 26 (a) Top and cross section view of HfZrO FTJ and (b) its current-voltage dependence [46].

Piezoelectricity, pyroelectricity, and electrocaloric-cooling (ECE) are physical phenomena known for many years. These physical effects were recently reconsidered due to the occurrence of considerable pyroelectric and ECE energy conversion in HfO_2-based ferroelectrics and antiferroelectrics [47]. A recent review discussing the performances of energy conversion and their dependence on temperature and doping concentrations is [48]. The energy storage density (ESD) is a parameter relevant for ferroelectric materials. The ESD is defined as:

$$ESD = \int_{Pr}^{P_{max}} EdP \quad (2)$$

where E is the electric field, P is the polarization, P_r the remanent polarization and P_{max} the maximum polarization. The energy storage efficiency is defined as:

$$\eta = ESD/(ESD + Loss) \quad (3)$$

In [48] it is noted that antiferroelectrics show a double hysteresis loop and lower losses compared to ferroelectrics, and thus attaining higher ESD.

Pyroelectricity means the generation of a current i when a temperature difference ΔT is applied to them. The ECE is the inverse effect of pyroelectricity, i.e., it describes the appearance of a difference in temperature ΔT when a current/voltage is applied.

The pyroelectric coefficient, with a value of -1300 $\mu C/m^2K$ in Si-doped HfO_2 ferroelectrics, was termed as giant in [47] and is the consequence of the temperature dependence of the concentration of ferroelectric phase near the phase transition between ferroelectricity and paraelectricity. This result has triggered further researches for CMOS compatible pyroelectric sensors having multiple applications in many industries, such as automotive, aerospace, and security. The research of CMOS compatible pyroelectric detectors has started decades earlier, when ferroelectric polymers were discovered. Based on these materials, large arrays of pyroelectric detectors, for example having 16×16 elements, were fabricated in CMOS technology [49] with very good performances, such as a pixel voltage sensitivity of 2200 V/W.

Recently, arrays of pyroelectric detectors based on Si-doped HfO_2 ferroelectric were designed, fabricated and measured. Because the pyroelectric current is given by:

$$i = pAdT/dt \quad (4)$$

where p is the pyroelectric coefficient, A is the device area, T is the temperature, and t is the time, the area of the sensor must be enhanced to obtain a higher current. One solution for increasing the sensor current is to use an array of pyroelectric sensors, as discussed above, or a micromachined Si array (see Fig. 27), of tens of millions of trenches [50],[51],[52]. In the last case, a current of few nA is generated when changing the temperature between 29 ^{o}C and 31^{o}C.

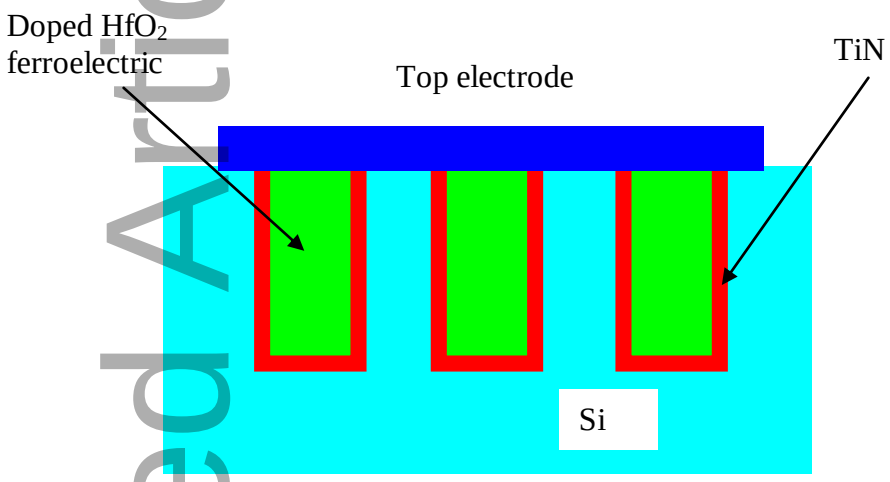

Fig. 27 The pyroelectric detector using doped HfO_2 ferroelectric based on Si micromachining.

The ECE effect was also termed as giant in the case of HfZrO, raising the hope for miniaturized solid-state refrigerators, which are key components in many industries where heat is produced. In particular, such devices are of interest for microprocessors, where for many years the dissipated heat is the main obstacle to increase significantly the performances [47],[53]. In the case of $Hf_xZr_{1-x}O_2$, if x = 0.2, 0.3, the ECE coefficient is positive, producing a ΔT of 10 K in a broad range of temperatures, 300-448 K. On the contrary, when x = 0.5 the ECE is negative and ΔT is 10.8 K at 448 K. However, the design and realization of a miniaturized ECE cooler are in infancy.

Any ferroelectric is also a piezoelectric material. Piezoelectricity, which refers to the transformation in a reverse manner of the mechanical energy into an electric current, is another

physical effect with many applications in energy harvesting (see the recent review [54]). In the case of HfO_2 ferroelectrics, the piezoelectricity is present in both thin and thick films [55], [56], [57] and the values of piezoelectric coefficients are similar to that of AlN. For example, a 1 μm-thick La-doped HfO_2 shows a d_{33} coefficient of 7.7 pm/V, while d_{33} for AlN is 6 pm/V. This fact opens new ways to use HfZrO-doped ferroelectrics for actuation applications, bulk acoustic wave resonators (BAW), and surface acoustic wave resonators (SAW), which are widespread in daily used electronic devices, such as smartphones and laptops.

6. The future of HfO_2-based ferroelectrics

Although the ferroelectricity in HfO_2 is a well-studied subject in many papers, the applications have a slower pace compared to material studies. Therefore, in the next years, nanoelectronics applications will emerge following the paths indicated above, i.e., they will concentrate on memories, low-power electronics circuits, tunable devices for wireless communications, sensors, and harvesting energy[58].

We note that the next-generation communication technologies (5G: 26-95 GHz by 2025 and 6G: 95 GHz-3 THz by 2030) have stringent requirements and as yet unsatisfied needs, such as: (i) low bias voltages for beam-steering capabilities; (ii) increased power efficiency and ultrafast switching times; (iii) miniaturization of wireless nodes; (iv) reconfigurability (to implement on-chip antenna multiplexing and antenna tuning); (v) frequency scalability (for future increase in bandwidth); (vi) zero-energy devices (built-in self-powering functionalities of mobile devices, such as Internet-of-Things (IoT) and Internet-of-Services (IoS)).

Presently, Si-based CMOS devices operate close to their theoretical limits in terms of power densities, operating frequencies, and temperature. Furthermore, traditional and current High-Frequency Electronics (HFE) technologies (III-V, GaN, and SiGe BiCMOS) are prohibitive for ultra-large volume manufacturing needs (50 billion mobile devices by 2030). Thus, none of the currently used materials and technologies can provide the above-mentioned requirements of low

power, ultra-fast switching times, reduced size, reconfigurability, and scalability. Therefore, the only way to achieve this goal is to use the quantum tunneling effect to build oxide-based high-frequency emitters and receivers working up to THz frequencies while being CMOS compatible. Therefore, HfO_2-based ferroelectrics could play a crucial role in the future 5G and 6G communication technologies due to CMOS compatibility and the versatility of physical properties obtained by doping engineering of materials.

Acknowledgments

This work was supported by UEFISCDI project number PN-III-P4-ID-PCCF-2016-0033 "GrapheneFerro", and European Union's Horizon 2020 FETPROACT grant agreement No 951761, "Nanomaterials enabling smart energy harvesting for next-generation Internet-of-Things" (NANO-EH).

References

[1] K. Kita, K. Kyuno, A. Toriumi, *Appl. Phys. Lett*. **2005**, *86*, 102906.

[2] K. Tomida, K. Kita, A. Toriumi, *Appl. Phys. Lett*. **2006**, *89*, 142902.

[3] S. Bang, S. Lee, S. Jeon, S. Kwon, W. Jeong, S. Kim, H. Jeon, *J. Electrochem. Soc*. **2008**, *155*, H633.

[4] T. S.Böscke, P. Y. Hung, P. D. Kirsch, M. A. Quevedo-Lopez, R. Ramírez-Bon, *Appl. Phys. Lett*. **2009**, *95*, 052904.

[5] M. H. Park, Y. H. Lee, H. J. Kim, Y. J. Kim, T. Moon, K. D. Kim, J. Muller, A. Kersch, U. Schroeder, T. Mikolajick, C. S. Hwang, *Adv. Mater*. **2015**, *27*, 1811.

[6] T. S. Böscke, J. Müller, D. Bräuhaus, U. Schröder, U. Böttger, *Appl. Phys. Lett*. **2011**, *99*, 102903.

[7] J. Müller, T. S Böscke, U. Schröder, S. Mueller, D. Braühaus, U. Böttger, L. Frey, T. Mikolajick, *Nano Lett*. **2012**, *12*, 4318.

[8] Y. Wei, P. Nukala, M. Salverda, S. Matzen, H. J. Zhao, J. Momand, A.S. Everhardt, G. Agnus, G. R. Blake, P. Lecoeur, B. J. Kooi, J. Íñiguez, B. Dkhil, B. Noheda, *Nature Materials* **2018**, *17*,1095.

[9] J. Ran, Z. Yan, *J. Semicond*. **2009**, *30*, 102002.

[10] N. H. Hong, in *Nano-sized Multifunctional Materials: Synthesis, Properties and Applications*, (Ed: N. H. Hong), Elsevier, Amsterdam, The Netherlands **2019**, Ch. 7.

[11] Z. Fan, J. Chen, J. Wang, *J. Adv. Dielectrics* **2016**, *6*, 1630003.

[12] T. Mimura, T. Shimizu, H. Funakubo, *Appl. Phys. Lett*. **2019**, *115*, 032901.

[13] S. S. Cheema, D. Kwon, N. Shanker, R. dos Rei, S.-H. Hsu., J. Xiao, H. Zhang, R. Wagner, A. Datar, M. R. McCarter, C. R Serrao, A. K. Yadav, G. Karbasian, C.-H. Hsu, A. J. Tan, L.-C. Wang, V. Thakare, X. Zhang, A. Mehta, E. Karapetrova, R. V. Chopdekar, P. Shafer, E. Arenholz., C. Hu., R. Proksch, R Ramesh, J. Ciston, S. Salahuddin, *Nature* **2020**, *580*, 478.

[14] M. Dragoman, M. Modreanu, I. M. Povey, S. Iordanescu, M. Aldrigo, C. Romanitan, D. Vasilache, A. Dinescu, D. Dragoman, *Nanotechnology* **2017**, *28*, 38LT04.

[15] S. J. Kim, J. Mohan, S. R. Summerfelt, J. Kim, *JOM* **2018**, *71*, 246.

[16] T. Shimizu, *J. Ceramic Soc. Japan* **2018**, *126*, 667.

[17] M. H. Park, Y. H. Lee, T. Mikolajick, U. Schroeder, C. S. Hwang, *MRS Commun*. **2018**, *8*, 795.

[18] M. A. Alam, M. Si, P. D. Ye, *Appl. Phys. Lett*. **2019**, *114*, 090401.

[19] M. Hoffmann, S. Slesazeck, U. Schroeder, T. Mikolajick, *Nature Electronics* **2020**, *3*, 504.

[20] J. C. Wong, S. Salahuddin, *Proc. IEEE* **2019**, *107*, 49.

[21] M. Dragoman, A. Dinescu, D. Dragoman, *Phys. Status Solidi A* **2019**, *216*, 1800724.

[22] C. Cui, W.-J. Hu, X. Yan, C. Addiego, W. Gao, Y. Wang, Z. Wang, L. Li, Y. Cheng, P. Li, X. Zhang, H. N. Alshareef, T. Wu, W. Zhu, X. Pan, L.-J. Li, *Nano Lett*. **2018**, *18*, 1253.

[23] Z. Guan, H. Hu, X. Shen, P. Xiang, N. Zhong, J. Chu, C. Duan, *Adv. Electron. Mater*. **2019**, *6*, 1900818.

[24] H. Ryu, K. Xu, D. Li, X. Hong, W. Zhu, *Appl. Phys. Lett*. **2020**, *117*, 080503.

[25] M. Dragoman, M. Aldrigo, D. Dragoman, I. M. Povey, S. Iordanescu, A. Dinescu, A. Di Donato, M. Modreanu, *Physica E* **2021**, *126*, 114451.

[26] A. Ahmed, I. A. Goldhorpe, A. K. Khandani, *Appl. Phys. Rev*. **2015**, *2*, 011302.

[27] M. Aldrigo, M. Dragoman, S. Iordanescu, F. Nastase, S. Vulpe, A. Dinescu, D. Vasilache, *IEEE Access* **2019**, *7*, 136686.

[28]

[29] M. Dragoman, M. Modreanu, I. M. Povey, S. Iordanescu, M. Aldrigo, A. Dinescu, D. Vasilache, C. Romanitan, *Electron. Lett*. **2018**, *54*, 469.

[30] M. Aldrigo, M. Dragoman, S. Iordanescu, F. Nastase, S. Vulpe, *Nanomaterials* **2020**, *10*, 2057.

[31] D. Martin, J. Müller, T. Schenk, T. M. Arruda, A. Kumar, E. Strelcov, E. Yurchuk, S. Müller, D. Pohl, U. Schröder, S. V. Kalinin, T. Mikolajick, *Adv. Mater*. **2014**, *26*, 8198.

[32] K. H. Lee, H.-J. Shin, J. Lee, I. Lee, G.-H. Kim, J.-Y. Choi, S.-W. Kim, *Nano Lett*. **2012**, *12*, 714.

[33] M. R. Amirzada, A. Tatzel, V. Viereck, H. Hillmer, *Appl. Nanosci*. **2016**, *6*, 215.

[34] G. A. Nemnes, D. Dragoman, M. Dragoman, *Phys. Chem. Chem. Phys*. **2019**, *21*, 15001,

[35] M. Dragoman, A. Dinescu, F. Nastase, A. Moldovan, D. Dragoman, *Nanotechnology* **2020**, *31*, 275202.

[36] M. Dragoman, A. Dinescu, F. Nastase, D. Dragoman, *Nanomaterials* **2020**, *10*, 1404.

[37] M. Dragoman, A. Dinescu, D. Dragoman, C. Palade, A. Moldovan, M. Dinescu, V. S. Teodorescu, M. L. Ciurea, *Nanotechnology* **2020**, *31*, 495207.

[38] S. G. Hu, S. Y. Wu, W. W. Jia, Q. Yu, L. J. Deng, Y. Q. Fu, Y. Liu, T. P. Chen, *Nanosci. Nanotechnol. Lett.*, **2014**, *6*, 729.

[39] C Tan, Z. Liu, W. Huang, H. Zhang, Non-volatile resistive memory devices based on solution-processed ultrathin two-dimensional nanomaterials, Chem. Soc. Rev.,**2015**,44, 2615–

[40] L. Zhang, T. Gong, H. Wang, Z. Guo, H. Zhang, *Nanoscale* **2019**, *11*, 12413.

[41] V. K. Sangwan, H.-S. Lee, H. Bergeron, I. Balla, M. E. Beck, K.-S. Chen, M. C. Hersam, *Nature* **2018**, *554*, 500.

[42] L. Wang, W. Liao, S. L. Wong, Z. G. Yu, S. Li, Y.-F. Lim, X. Feng, W. C. Tan, X. Huang, L. Chen, L. Liu, J. Chen, X. Gong, C. Zhu, X. Liu, Y.-W. Zhang, D. Chi, K.-W. Ang, *Adv. Funct. Mater.* **2019**, *29*, 1901106.

[43] J. Jadwiszczak, D. Keane, P. Maguire, C. P. Cullen, Y. Zhou, H. Song, C. Downing, D. Fox, N. McEvoy, R. Zhu, J. Xu, G. S. Duesberg, Z.-M. Liao, J. J. Boland, H. Zhang, *ACS Nano* **2019**, *13*, 14262.

[44] C. Liu , H. Chen , X. Hou, H. Zhang, J. Han, Y.-G. Jiang, X. Zeng, D. W. Zhang, P. Zhou , *Nature Nanotechnol.* **2019**, *14*, 662.

[45] M. K. Mishu, M. Rokonuzzaman, J. Pasupuleti, M. Shakeri, K. Sajedur Rahman, F. A. Hamid, S. K. Tiong, N. Amin, *Electronics* **2020**, *9*, 1345.

[46] M. Aldrigo, M. Dragoman, M. Modreanu, I. Povey, S. Iordanescu, C. Romanitan, D. Vasilache, A. Dinescu, D. Masotti, M. Shanawani, *IEEE Trans. Electron Dev.* **2018**, *65*, 2973.

[47] M. Dragoman, M. Modreanu, I. M. Povey, M. Aldrigo, A. Dinescu, D. Dragoman, *Nanotechnology* **2018**, *29*, 445203.

[48] M. Hoffmann, U. Schroeder, C. Künneth, A. Kersch, S. Starschichc, Ulrich Böttgerc, T. Mikolajicka, *Nano Energy* **2015**, *18*, 154.

[49] F. Ali, D. Zhou, M. Ali, H. W. Ali, M. Daaim, S. Khan, M. M. Hussain, N. Sun, *ACS Appl. Electron. Mater.* **2020**, *2*, 2301.

[50] T. D. Binnie, H. J. Weller, Z. He, D. Setiadi, *IEEE Trans. Ultrasonics, Ferroelectrics, Freq. Control* **2000**, *47*, 1414.

[51] C. Mart, W. Weinreich, M. Czernohorsky, S. Riedel, S. Zybell, K. Kühnel, CMOS compatible pyroelectric applications enabled by doped HfO_2 films on deep-trench structures, in *Proc. 48th European Solid-State Device Research Conference (ESSDERC 2018)*, IEEE, USA **2018**, 130.

[52] B. Hanrahan, C. Mart, T. Kämpfe, M. Czernohorsky, W. Weinreich, A. Smith, *Energy Technol.* **2019**, *7*, 1900515.

[53] C. Mart, A. Viegas, M. Czernohorsky, W. Weinreich., A. Kaiser, N. Neumann, T. Großmann, K. Hiller, L. M. Eng, Pyroelectric CMOS compatible sensor element based on hafnium oxide thin films, in *Proc. 2020 Joint Conf. of the IEEE International Frequency Control Symposium and International Symposium on Applications of Ferroelectrics (IFCS-ISAF)*, IEEE, USA **2020**, 1.

[54] M. H. Park, H. J. Kim, Y. J. Kim, T. Moon, K. D. Kim, Y. H. Lee, S. D. Hyun, C. S. Hwang, *Adv. Mater.* **2016**, *28*, 7956.

[55] G. Zhang, M Li, H. Li, Q. Wang, S. Jiang, *Energy Technol*. **2018**, *6*, 791.

[56] T. Schenk, N. Godard, A. Mahjoub, S. Girod, A. Matavz,, V. Bobnar, E. Defay, S. Glinsek, *Phys. Status Solidi-RRL* **2020**, *14*, 1900626.

[57]C. Mart, T. Kämpfe, R. Hoffmann, S. Eßlinger, S. Kirbach, K. Kühnel, M. Czernohorsky, L. M Eng, W. Weinreich „Piezoelectric Response of Polycrystalline Silicon-Doped Hafnium Oxide Thin Films Determined by Rapid Temperature Cycles" Advanced Electronic Materials 3, 1901015 (2020)

[58]M.Dragoman and D.Dragoman, Electronics at atomic scale beyond CMOS, Springer. Cham ,Switzerland, 2021.

This paper is dedicated to the HfO_2-based ferroelectrics applications in nanoelectronics especially in topics not very developed up to now such as microwaves, energy harvesting, and neuromorphic devices working as artificial neurons and synapses. The transfer of 2D materials on HfO_2

ferroelectrics has demonstrated new physical effects such as the opening of the bandgap in graphene monolayers of 0.2 eV, and very high mobility of FETs based on graphene/HfZrO.

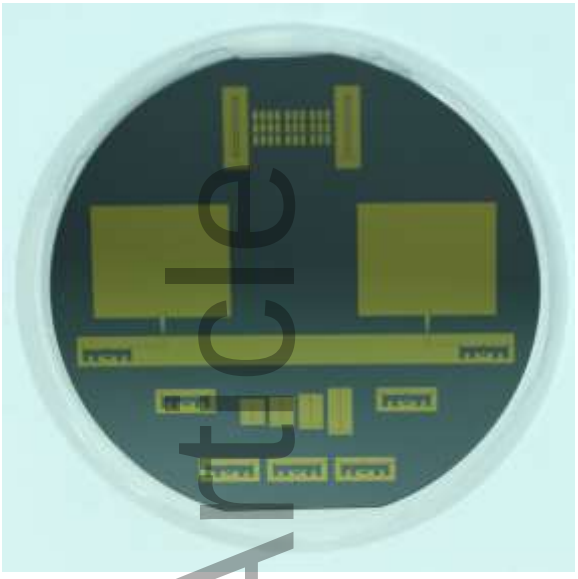

Mircea Dragoman is Senior Researcher I with the NationalResearch Institute in Microtechnologies (IMT), Romania where is the director of the Reseach Center of Carbon based Nanotechnologies.He is co-author of more than 300 scientific papers and 7 books published at Springer and Artech House (USA) in the area of nanoelectronics, optics and quantum mechanics.

Martino Aldrigo received the Ph.D. in Electronics Engineering, Telecommunications and Information Technology in 2014 from the Faculty of Engineering, University of Bologna, Italy. Since 2014, he is Principal Researcher III with IMT-Bucharest, Romania.

His main expertise comprises the electromagnetic simulation and experimental characterization of RF/microwave/millimeter-wave/THz systems for wireless/energy-harvesting applications. He has co-authored more than 60 papers in ISI ranked journals and conferences. He is an IEEE member. He serves or has served as reviewer for many journals and as (co-)chair in international conferences.

Daniela Dragoman received the M. Sc. degree in semiconductor physicsfrom the Faculty of Physics, University of Bucharest, Romania, in1989, and the Ph.D. degree in optoelectronics from the Universityof Limerick,

Ireland, in 1993. Between 1998–1999 and 2001–2002she was the recipient of the Humboldt Fellowship award and hasfollowed postdoctoral studies at University of Mannheim,Germany. She is presently Professor with the Faculty ofPhysics, University of Bucharest.

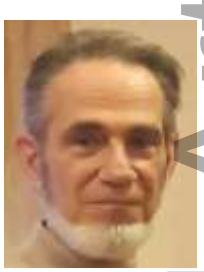

Sergiu Iordanescu (M'91) received the Ph.D. degree in electronic engineering from the University "Politehnica" Bucharest, Romania in 2000. He is Senior Researcher II with IMT-Bucharest, Romania.
His research interests include microwave SAW filter, sensor and microwave/millimeter wave circuits design and characterization, dielectric and ferroelectric materials characterization. He is the author of more than 100 scientific papers in peer-reviewed journals and conferences. He received the "Tudor Tanasescu" Romanian Academy award (with team) for the study "Micromachined circuits for microwave and millimeter wave applications – MEMSWAVE".

Dr. Adrian Dinescu obtained the MSc and PhD degrees in solid state physics both from Faculty of Physics, University of Bucharest. Between 1993 and 1997, he was with the National Institute for Electronic Components Research, working in the field of optoelectronics. Since 1997 he is with IMT-Bucharest, currently being CEO and President of the Board. Adrian Dinescu was the head of Nanoscale Structuring and Characterization Laboratory for seventeen years and Technical Manager of IMT for five years. Dr.Dinescu is involved in the micro and nanoscale characterization using FE-SEM and in structuring at the nanoscale using Electron Beam Lithography. His expertise also includes: micro and nanofabrication and optoelectronic measurements. He has co-authored more than 100 papers in refereed international journals and coordinated 15 national and 3 European research projects.

Mircea Modreanu received an M.Sc. (1993) and a Ph.D. (2002) in Condensed matter physics from the Faculty of Physics, University of Bucharest, Italy. From 1993 until 2002 held a Senior Researcher position in IMT-Bucharest, Romania. In 2002 he joined Tyndall National Institute-University College Cork, Ireland as Principal Investigator.

His main expertise comprises nanomaterials development for micro-nano electronics, nanophotonics, and RF/microwave/millimeter-wave/ systems for wireless/energy-harvesting applications. He has co-authored more than 140 papers in ISI-ranked journals and conferences. He was organized several international conferences in Europe and Japan in the area of optical and x-ray metrology advanced materials for nanoscale devices.